Research Article

Effects of Material Rheology and Die Walls Translational Motions on the Dynamics of Viscous Flow during Equal Channel Angular Extrusion through a Segal 2θ-Die: CFD 2D Solution of a Curl Transfer Equation

Alexander V. Perig[1] and Nikolai N. Golodenko[2]

[1]*Manufacturing Processes and Automation Engineering Department, Donbass State Engineering Academy, Shkadinova Str. 72, Kramatorsk 84313, Ukraine*
[2]*Department of Water Supply, Water Disposal and Water Resources Protection, Donbass National Academy of Civil Engineering and Architecture, Lazo Str. 14, Kramatorsk 84333, Ukraine*

Correspondence should be addressed to Alexander V. Perig; olexander.perig@gmail.com

The present article is focused on a phenomenological description of a polymer workpiece Equal Channel Angular Extrusion (ECAE) through 2θ-dies of Segal and Iwahashi geometries with a channel intersection angle $2\theta = 105°$ with fixed and movable external inlet and outlet die walls. The local flow dynamics, including the formation of macroscopic rotation and a dead zone appearance during the flow of plasticine, paraffin, and wax workpiece models through the subject die configuration was studied using physical simulation techniques. The present article utilizes a Computational Fluid Dynamics (CFD) numerical approach to a theoretical description of 2D viscous flow of incompressible Newtonian continuum through the stated die geometries. The boundary value problem for the Navier-Stokes equations in the curl transfer form for the local viscous flow was formulated and numerically solved with a finite-difference method. Theoretical CFD-derived plots with computational flow lines, dimensionless flow and curl functions, flow velocities, and tangential stresses for viscous material flow through the stated die geometries have been generated and described. As a first rheological approximation the derived computational results provide the theoretical description of physical simulation experiments and visualize the formation of ECAE-induced rotational modes of large deformations like macroscopic rotation and rotational inhomogeneity.

1. Introduction and Background

In recent years materials science and materials pressure working [1–27] also deal with the continuum mechanics-based description of the dynamics of macroscopic and microscopic phenomena in the rheologically complex composite and polymeric systems under external perturbations of pressure worked materials [1–5, 7–9, 13, 14, 17, 19–34]. Macroscopic phenomenological description of local materials flow within polymeric systems under external working by pressure is closely associated with modern problems of nonequilibrium thermodynamics of irreversible processes, classical continuum mechanics, Computational Fluid Dynamics (CFD) [9, 13, 14, 17, 19, 20, 30, 32, 34, 35], rheodynamics and rheology [29], rheomechanics and rheophysics [30], polymer physics and chemistry [32, 34], material kinetics [31], complex macromolecule networks, chemical engineering of polymers, chemical technology of complex fluids, material working by pressure [1–27], medical applications, and phenomenological continuum-based theories of polymer viscous flow [29–32, 34]. So the rheodynamics and rheology of polymer pressure working is also within the aims and scopes of such

Severe Plastic Deformation (SPD) problems as Equal Channel Angular Extrusion (ECAE) or Equal Channel Angular Pressing (ECAP). The forming processes of SPD by ECAE also find applications in iron and steel industry, nonferrous metals industry, chemical and mechanical engineering for pressure working of alloys, composites, metals, and polymer and powder workpieces.

ECAE (ECAP) is based on one or several extrusion (pressing) passes of a lubricated metal or polymer worked material through the angular die with two intersecting inlet and outlet channels of equal cross-section. ECAE-induced pressure forming of worked materials results in the getting, accumulation, and redistribution of large plastic shear strains and structure refinement of processed material with substantial enhancement of physical and mechanical properties.

The observable macroscopic dynamics of the ECAE (ECAP) technological process is characterized by emerging essential plastic strain inhomogeneity and unevenness, nonuniformity of large strain redistribution, appearance of macroscopic rotation and rotational modes of SPD both within the deformation zone and workpiece volume in the outlet die channel, and the formation of a dead zone in the die channel intersection zone of the workpiece local flow. These phenomena lead to a further development and propagation of SPD rotational modes and macroscopic rotation within the volume of pressure worked material and a decrease in length for the workpiece areas with stationary local viscous flow and an increase in material waste due to normal truncation of extruded material between successive ECAE passes. Strain inhomogeneity, unevenness of deformation distribution, and plastic strain nonuniformity are also factors, which reduce the final yield of workpiece formed material during multiple passes of SPD by ECAE. Recent publications indicate essential scientific interest in a qualitative and quantitative experimental-theoretical description of the phenomenological dynamics of SPD and formation of associated pressure-induced rotational modes like macroscopic rotations and rotational inhomogeneity within pressure worked materials during ECAE.

Today rheologically complex problems of pressure-induced polymer dynamics during SPD by ECAE attract the attention of such researchers as Aour et al. (2009) [1], Beloshenko et al. (2013) [2], Boulahia et al. (2009) [3], Creasy and Kang (2004) [4], Han et al. (2008) [5], Li et al. (2012) [7], Minakowski (2014) [8], Perig et al. (2010, 2014–2016) [9, 13, 14, 17, 19, 20], Qiu et al. (2012) [21], Seo and Weon (2013) [22], Sue et al. (1999) [23], Weon et al. (2005) [24], Xia et al. (2000) [26], Zhang et al. (2008) [27], and others. Research efforts of these scientists have been focused on physical-mechanical investigations into the engineering problems of polymer materials local flow in angular domains during SPD ECAE material pressure forming.

2. The State of the Art

Aour et al. (2009) have used MSC's FEA proprietary software MSC.Marc to numerically model local flow of a high-density polyethylene workpiece through a generalized Iwahashi-geometry angular die with a right angle $2\theta = 90°$ channel intersection and external and internal radii in channel intersection zone and with Coulomb's friction law between the polymer workpiece model and the die walls [1]. The advantage of Aour et al.'s (2009) approach includes the availability of experimental-theoretical analysis of multipass ECAE using different deformation routes [1]. However Aour et al.'s (2009) phenomenological research does not fully address the macroscopic dynamics of formation and development of rotational modes of ECAE-induced large deformations during pressure-driven local flow of HDPE and PE polymer workpieces [1].

Beloshenko et al.'s (2013) review research has analyzed and systematized the change of the structure of glassy polymers, polymer composites and semicrystalline polymers under the action of SPD ECAE-induced large deformations [2]. It is very sound that Beloshenko et al. (2013) have addressed a wide range of technological, physical, and chemical aspects of polymer pressure forming by ECAE through angular and multiple-angular dies [2]. However, Beloshenko et al. (2013) have not fully addressed the kinematic influence of movable die walls of ECAE die tooling on the dynamics of local flow of polymer workpieces [2]. Mesomechanics and macromechanics of rotational modes formation in pressure worked polymer materials were also beyond the scope of Beloshenko et al.'s (2013) review study [2].

Boulahia et al. (2009) have analyzed the influence of ECAE back-pressure and ECAE punching velocity on the energy-power parameters of polymer workpiece local flow through an angular die of Iwahashi geometry [3]. The experimentally enhanced visualization of the effects of ECAE back-pressure and ECAE punching speed on the geometric shape of pressure formed polymer workpieces has been provided in the valuable contribution [3] by Boulahia et al. (2009). However Boulahia et al.'s (2009) research did not fully address the physical mechanisms of SPD, which caused formation of macroscopically observable defects of polymer workpieces of wavy shape [3]. Macroscopic and microscopic experimental studies by Boulahia et al. (2009) have not been focused on visualization of macroscopic and microscopic rotations and rotational SPD modes within volume of ECAE-driven polymer workpieces [3].

Creasy and Kang (2004) did experimental research of ECAE-stipulated local flow of a polyacetal rod-shaped workpiece through an angular domain of Segal geometry with a right angle $2\theta = 90°$ channel intersection [4]. A wide range of experimentally originated plots, derived during processing of experimental results, is among obvious advantages of Creasy and Kang's (2004) research [4]. However Creasy and Kang (2004) have not produced photos of their experimentally derived results that really complicate estimation of effect of SPD-induced rotary modes on fiber orientation within pressure worked polymer workpiece [4]. Moreover, Creasy and Kang's (2004) research contains no mention of the appearance or experimental investigation of rotational modes of SPD during ECAE-driven pressure forming of thermoplastic workpiece [4].

Han et al. (2008) have applied physical simulation techniques for experimentally enhanced visualization of empirical flow lines during ECAE through an Iwahashi die by using color grains at the front surface of the extruded workpiece [5].

Han et al. (2008) have proposed simple geometric equations for material flow lines within the deformation region during ECAE of worked material through Segal-geometry die with channel intersection angle 90° [5]. Han et al. (2008) have derived phenomenological equations of flow lines as the piecewise functions with an assumption that material flow lines are composed of two straight lines in the vertical inlet and horizontal outlet die channels and one symmetric circular arc in the region of the central segment, which restricts the symmetric dead zone in the channel intersection region [5]. However the local flow of color grains in Han et al.'s (2008) ECAE experiments has a rheologically complex nature [5]. Therefore, empirically enhanced Han et al.'s (2008) phenomenological approach to ECAE flow lines geometric description is a rather simplified one [5]. Factually Han et al. (2008) have not addressed the differential equations, which theoretically determine the experimentally observable flow lines during local flow of the grained material through the ECAE die [5]. Therefore, Han et al. (2008) decided a priori to set the shape of material flow lines during ECAE trying graphically to guess the numerical integral instead of doing an accurate formulation and the further numerical solution of unknown differential equations for local ECAE-stipulated flow of grained material [5].

Li et al. (2012) have performed empirical investigations of multipass ECAE-caused local flow of a solid phase polymer nanocomposite workpiece, produced from polypropylene and organic montmorillonite, through an angular die of Segal geometry with a right angle $2\theta = 90°$ channel intersection [7]. Li et al. (2012) have provided experimental optically and TEM-derived photos of microslices of pressure worked polymer workpieces, which illustrate ECAE-assisted polymer structure fragmentation [7]. However Li et al. (2012) did not fully address the physical mechanisms, which govern the generation, appearance, growth, and development of rotational modes of SPD that are responsible for macroscopic rotation, mixing, crashing, fragmentation, and structural refinement of polymer workpieces within the deformation zone [7].

Minakowski (2014) has numerically studied ECAE-driven flow of polymer material with a density of 3000 kg/m^3 through a multiple-angled two-turn S-shaped die of generalized Iwahashi geometry [8]. Minakowski (2014) has used CFD-techniques and continuum mechanics-based governing equations together with FEniCS FEM freeware [8]. However, Minakowski's (2014) approach did not address additional kinematic effects, associated with independent translational motions of movable die walls during ECAE through the S-shaped multiple-angled die [8].

Perig et al., 2010, 2014–2016, have applied a continuum mechanics-based approach and fluid dynamics techniques for simple phenomenological description of growth, formation and transformation of rotational modes of large deformations (e.g., macroscopic rotation and rotational inhomogeneity) within the volume of a viscous workpiece model in the process of ECAE [9, 13, 14, 17, 19, 20]. Finite-difference-based 2D computer hydrodynamic modeling of viscous ECAE flows of incompressible fluid through angular domains with different die geometries [9, 13, 14, 17, 19, 20] was based on the difference approximation and numerical

solution of curl (vorticity) transfer form of the Navier-Stokes difference equations with an introduction of the curl (vorticity) and flow (stream) function formulation [9, 13, 14, 17, 19], and flow velocities punching pressure formulation [20]. Computational diagrams of flow lines and flow velocities for correspondent ECAE-stipulated flows have been determined with an application of Computational Fluid Dynamics (CFD) modeling to flow of viscous fluids through the angular and multiple-angular dies [9, 13, 14, 17, 19, 20].

Perig et al. (2010) have applied an experimental-theoretical approach to a phenomenological continuum mechanics-based description of polymer workpiece viscous flow through an angular domain of Segal geometry with a right angle $2\theta = 90°$ die channel intersection through a numerical CFD-based solution of Navier-Stokes equations in curl (vorticity) transfer form [9].

Perig and Golodenko (2014) have analyzed local features of a plasticine-based long combined workpiece model during ECAE through a multiple-angle S-shaped angular domain with a translationally movable inlet die wall through the joint usage of physical simulation techniques and a CFD-based solution of Navier-Stokes equations in curl (vorticity) transfer form with respect to the variables, the curl (vorticity), and flow (stream) function [13].

Perig and Golodenko (2014) have performed experimental-theoretical studies of the formation of flow patterns and development of rotational modes of deformation during local flow of viscous fluid through a multiple-angled die domain in the shape of vertical inlet die channel, horizontal outlet die channel with a right angle $2\theta = 90°$ inlet, and outlet channel intersection and with an inclined plane transition channel (parallel slants), connecting the inlet and outlet die channels [14].

Perig et al. (2015) have investigated the effect of $2\theta_0$-punch shape on the dynamics of local flow during ECAE of plasticine models of worked materials through the 2θ-angular dies for the cases of $2\theta_0 = 2\theta$ and $2\theta_0 = 90°$ for plastic [16] and viscous [17] flows of metal [16] and polymer [17] workpiece models.

Perig and Golodenko (2016) have addressed the technological problem of angular extrusion of viscous continuum through a multiple-angled U-shaped angular die with an application of physical simulation and CFD techniques [19].

Perig and Golodenko (2016) have analyzed ECAE-driven viscous flow through an angular die of Segal geometry with $2\theta = 90°$ through a direct numerical solution of the Navier-Stokes equations with respect to the physical variables "flow velocities u, v of viscous flow and ECAE punching pressure p" [20].

Qiu et al. (2012) have performed an experimental investigation of the dynamics of spherulite fragmentation during local ECAE plastic flow of a crystalline polypropylene workpiece through an angular domain of Segal geometry with a right angle $2\theta = 90°$ channel intersection [21]. Qiu et al. (2012) have applied microscopy-enhanced experimental analysis of polished microsections of an ECAE-stipulated pressure formed workpiece for visualization of polymer structure fragmentation by destructive assistance of rotational deformation modes of SPD at microlevel of pressure worked

polymer material [21]. The research [21] provides additional processing of Qiu et al.'s (2012) experimental results with 2D graphical plots for changes in polymer molecular orientation in different workpiece cross-sections during ECAE [21]. However, Qiu et al. (2012) have not provided experimental vector fields for illustration of polymer material macroscopic rotation within deformation zone during ECAE processing [21].

Seo and Weon (2013) have outlined and analyzed the experimental influence of ECAE die geometry and the type of multipass ECAE deformation route on the microlevel dynamics of polyamide-6 structure fragmentation during local flow of polyamide-6/clay composite through an angular domain of Segal geometry with a right angle $2\theta = 90°$ channel intersection [22]. Seo and Weon (2013) have plotted additional experimentally derived schematic diagrams and TEM images for the illustration of macroscopic rotation of material elements within pressure worked polymeric material during multipass ECAE processing [22]. However, Seo and Weon's (2013) research has not provided additional plots for generalization of their ECAE route-dependent results [22].

Sue et al. (1999) have performed experimental-theoretical studies of a local ECAE-induced flow of polycarbonate plate workpieces through an angular domain of Segal geometry with a right angle $2\theta = 90°$ die channel intersection [23]. Experimental studies by Sue et al. (1999) have included such experimental parameters as a rate of angular extrusion, die channel angle, and a deformation route of multipass pressure working of polymer workpiece [23]. Sue et al. (1999) have visualized deformation gradients during ECAE-induced polymer flow through the application of Abaqus software [23]. However Sue et al. (1999) have not fully outlined FEM and experimentally derived fields of deformation gradients that significantly reduce generalization of experimental-theoretical research results of [23].

Weon et al. (2005) have analyzed the influence of deformation route of ECAE on ballistic impact properties of polymethylmethacrylate workpieces, subjected to pressure working through an angular domain of Segal geometry with a right angle $2\theta = 90°$ die channel intersection [24]. Weon et al. (2005) have provided an experimental photo of ECAE die tooling and a series of photographs and micrographs, which illustrate ECAE-induced polymer structure fragmentation as well as mechanical effects of improvement of ballistic impact polymer properties after ECAE pressure working [24]. However in the theoretical studies of [24] Weon et al. (2005) have used the well-known Segal's formulae for ECAE-induced plastic shear strains, which were proposed for ECAE pressure working of metals but not polymers, which slightly reduces the generality of the research [24].

Xia et al. (2000) have applied a wide range of experimental techniques for analysis and visualization of structure fragmentation of polyethylene terephthalate workpieces after different deformation routes of a multipass ECAE through an angular domain of Segal geometry with a right angle $2\theta = 90°$ die channel intersection [26]. Xia et al. (2000) have provided a comprehensive experimental investigation of the refinement of lamellar polymer structure during ECAE with corresponding experimentally derived 2D and 3D plots,

illustrating macroscopic and microscopic effects, associated with polymer workpiece fragmentation [26]. However, Xia et al. (2000) only partially addressed the questions of ECAE-driven macroscopic rotation formation [26].

Zhang et al. (2008) have applied experimental techniques to a technological problem of warm ECAE pressure forming and consolidation of polymer workpieces using wheat starch and wheat gluten granular materials through a classical Segal die with $2\theta = 90°$ with an additional back pressure [27]. Zhang et al. (2008) have provided dynamic mechanical analysis-related plots and scanning electron microscope-derived polymer microstructures after ECAE working by pressure. However, Zhang et al.'s (2008) contribution has not properly address the formation of rotational modes of ECAE-induced large deformations.

3. Aims, Scopes, and Prime Novelty of the Article

Analysis of the state of the art in the field of ECAE polymer forming shows that SPD ECAE problems are relatively new for the SPD and polymer sciences. For the last 17 years ECAE polymer forming science has attracted the attention of specialists in experimental and computational materials science and materials rheology. However all previous pressure forming research [1–27] pays inadequate attention to the dynamics of viscous flow of polymer workpiece models during ECAE through 2θ angular dies of Segal and Iwahashi geometries. Moreover the experimental and theoretical dynamics of macroscopic rotation formation during ECAE is still not properly addressed in all previous known publications [1–35]. All of the above mentioned references and discussion emphasize the relevance and actuality, the aims and scopes, and the prime novelty statement of the present research, which is focused on the experimental and theoretical description of material macroscopic rotation during ECAE of viscous polymer models in terms of continuum mechanics and CFD theories.

The present article is focused on the experimental and theoretical description of viscous workpiece flow through 2θ angular dies of Segal and Iwahashi geometries during ECAE.

The aim of the present research is the phenomenological continuum mechanics based description of viscous workpiece flow through 2θ angular dies of Segal and Iwahashi geometries with fixed and movable inlet and outlet die walls during ECAE.

The subject of the present research is the process of ECAE through 2θ angular dies of Segal and Iwahashi geometries with viscous flow of polymeric workpiece models and independent translational motions of movable inlet and outlet die walls of angular domain.

The object of the present research is to determine the general trend of viscous flow of workpiece models through 2θ angular dies of Segal and Iwahashi geometries with fixed and movable inlet and outlet die walls with respect to workpiece material rheology and other technological parameters of ECAE process.

The experimental novelty of the present article is based on the introduction of initial circular gridlines to study

(a)

(b)

(c)

(d)

(e)

(f)

FIGURE 1: The flow of physical plasticine models of polymer materials through an ECAE die AOC–BED of Segal geometry with channel intersection angle ∠(BED) = ∠(AOC) = 2θ = 105°: (a), (b), (c) the flow of uniform plasticine workpieces; (d) the flow of plasticine workpiece with additional solid markers at the front surface of workpiece in the shape of the hard spots; (e), (f) the flow of plasticine workpieces with additional dispersed particles on the front surfaces of workpieces in the form of partially immersed fine sawdust.

viscous workpiece ECAE flow through 2θ angular dies of Segal geometry.

The prime novelty of the present research is the numerical finite-difference solution of Navier-Stokes equations in the curl transfer form for viscous workpiece flow through 2θ angular dies of Segal and Iwahashi geometries with fixed and movable inlet and outlet die walls during ECAE.

4. Physical Simulation-Based Phenomenological Approach

In order to estimate the character of viscous flow during ECAE through the 2θ angular die of Segal geometry AOC–BED (Figures 1 and 2), a physical simulation technique has been applied. The plasticine workpiece models have been extruded through the ECAE die AOC–BED with channel
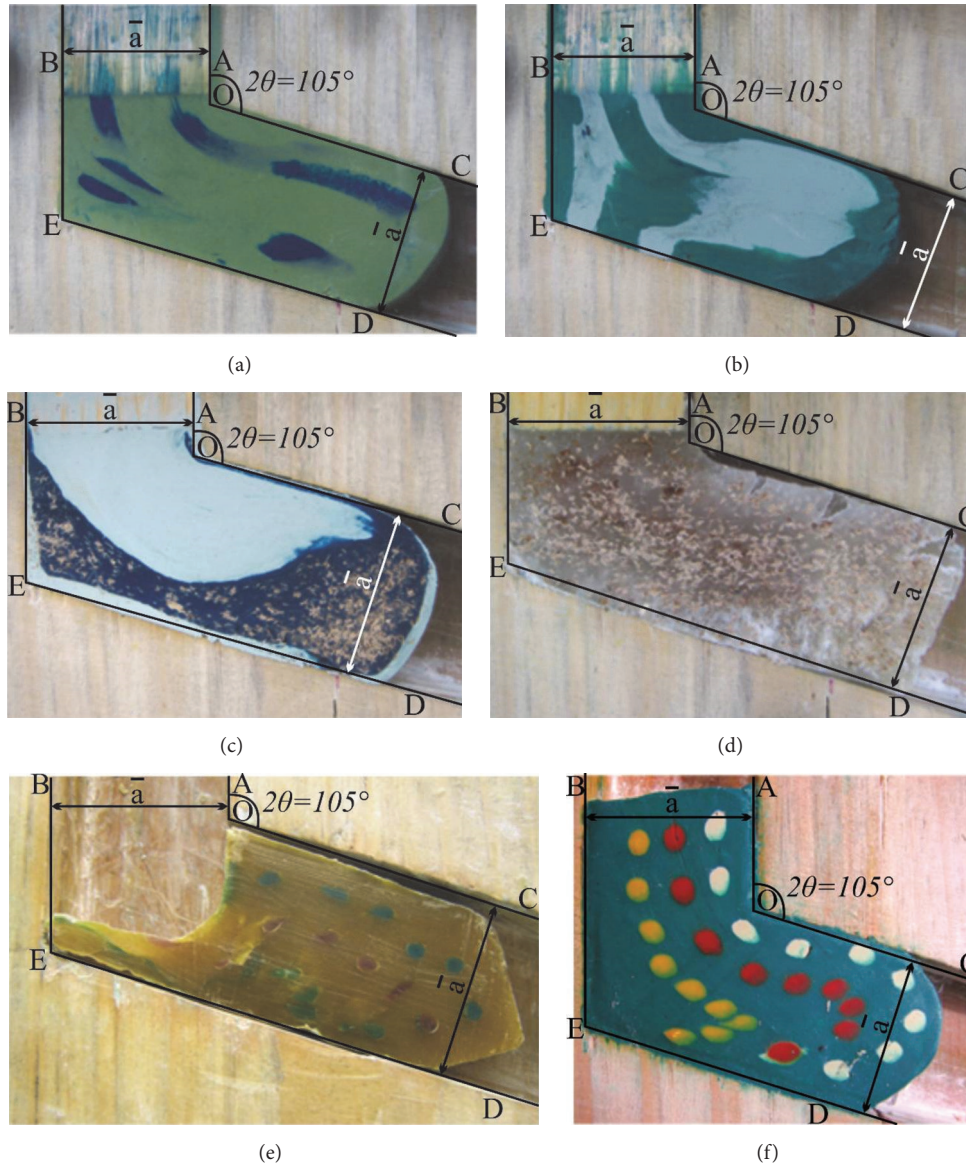
(a)

(b)

(c)

(d)

(e)

(f)

FIGURE 2: The flow of physical plasticine ((a), (b), (c), (f)), paraffin (d), and wax (e) models of polymer materials through the equal channel angular die AOC–BED of Segal geometry with channel intersection angle ∠(BED) = ∠(AOC) = 2θ = 105°: (a), (b), (c) the flow of layered plasticine models; (d) the flow of a paraffin workpiece with additional dispersed particles at the front surface of the workpiece in the form of partially immersed fine sawdust; (e) the flow of the yellow wax workpiece with the initial circular colored gridlines in the shape of the initial colored cylindrical wax inclusions with blue, red and green colors; (f) the flow of the blue plasticine workpiece with the initial circular colored gridlines in the shape of initial colored cylindrical plasticine inclusions with white, red, and yellow colors.

intersection angle ∠(BED) = ∠(AOC) = 2θ = 105° as the first experimental approach to polymeric materials flow (Figures 1 and 2).

The aim of physical simulation is an experimental study of dead zone formation in p. E and deformation zone location during viscous ECAE flow of workpiece plasticine models. The physical simulation in Figures 1 and 2 is also focused on the experimental visualization of rotary modes of SPD during ECAE of viscous polymer models.

The experimental results in Figures 1 and 2 are the original experimental research results, obtained by authors of the present article.

The wood die model of ECAE die AOC–BED with channel intersection angle ∠(BED) = ∠(AOC) = 2θ = 105° and the inlet AB and outlet CD die channel width 15 mm is shown in Figures 1 and 2. Initially, the uniform plasticine material workpiece models were extruded (Figures 1(a)–1(c)). Potato flour was used as the lubricator in Figures 1(a)–1(c). It was found that the dead zone (p. E) formation takes place in the vicinity of the external angle BED of channel intersection zone EO.

It was experimentally shown that a better visualization of the dead zone (p. E) formation during ECAE is available by introducing additional dispersed particles at the front

surfaces of workpieces in the form of partially immersed fine sawdust (Figures 1(e), 1(f), and 2(d)). The best visualization of the dead zone (p. E) formation is shown in Figure 1(f). The next experimental approaches to the visualization of the dead zone (p. E) formation during viscous ECAE flow are shown in Figures 2(a)–2(c), which additionally confirm the dead zone (p. E) location near the external obtuse angle BED within die channel intersection zone OE during extrusion of the layered plasticine models.

However, in order to outline the deformation zone (p. E) location, the initial circular gridlines technique was applied, shown in experimentally derived Figures 2(e) and 2(f).

The main experimental visualization technique in Figures 2(e) and 2(f) is based on the manufacture of the initial wax (Figure 2(e)) and plasticine (Figure 2(f)) physical models of the workpieces in the shapes of rectangular parallelepipeds, freezing these shapes, marking the initial circular gridlines on the front sides of frozen shapes, perforating the through-holes in the shapes at the centers of the initial circular gridlines, repeated freezing of the wax (Figure 2(e)) and plasticine (Figure 2(f)) shapes, heating the wax (Figure 2(e)) and plasticine (Figure 2(f)) pieces with different colors to the half-solid state, and placing the half-solid multicolor wax (Figure 2(e)) and plasticine (Figure 2(f)) into through-holes of the frozen shapes through the application of squirt without needle. In this way the initial wax-based (Figure 2(e)) and plasticine-based (Figure 2(f)) circular gridlines were marked throughout the initial wax (Figure 2(e)) and plasticine (Figure 2(f)) workpieces.

The initial circular gridline transforms into a deformed elliptical one as the workpiece flows from the inlet to outlet die channels during ECAE (Figures 2(e) and 2(f)). The gridline-free dead zones (p. E) were visualized through the physical simulation techniques introduced in Figure 2(f). It was experimentally found in Figures 2(b), 2(c), 2(e), and 2(f) that the deformation zone during ECAE of viscous models is not located in channel intersection zone EO but is located in the beginning of the outlet die channel OCED.

The relative location of the elliptical markers in the outlet die channel OCED shows the formation of two rotary modes of SPD during ECAE (Figures 2(e) and 2(f)). If the successive locations of one color elliptical markers in Figures 2(e) and 2(f) are checked, it can be seen that the major axis of every elliptical marker rotates with respect to the axis of the outlet die channel OCED. The term of macroscopic rotation is defined as the relative rotation of the major axis of the elliptical marker with respect to the flow direction axis. The macroscopic rotation is the first visually observable rotary mode during the ECAE forming of the viscous workpiece model. However, under SPD ECAE treatment some deformed elliptical markers within the viscous material have obtained additional bending points in the form of "commas" or "tadpoles" (Figure 2(e)). If the elliptical marker has a bending point during ECAE, then we refer to the vicinity of a marker with such a "waist" as the zone of rotational inhomogeneity within the workpiece material. The rotational inhomogeneity is the second visually observable rotary mode during ECAE forming of the viscous workpiece model.

The experimental results in Figures 1 and 2 have outlined the formation of the following zones within the workpiece volumes: (a) the dead zone (p. E); (b) the deformation zone; (c) the macroscopic rotation zone (OCED); and (d) the zone of rotational inhomogeneity (OCED). The complex physical simulation techniques in Figures 1 and 2 include the following experimental methods: (a) the uniform plasticine workpieces (Figures 1(a)–1(c)); (b) the plasticine workpiece with additional solid markers at the front surface of the workpiece in the form of the hard spots (Figure 1(d)); (c) the uniform plasticine and wax workpieces with additional dispersed particles at the front surfaces of the workpieces in the form of the partially immersed fine sawdust (Figures 1(e), 1(f), and 2(d)); (d) the layered plasticine models (Figures 2(a) and 2(b)); (e) the wax and plasticine workpieces with the initial circular colored gridlines in the shape of initial colored cylindrical plasticine inclusions (Figures 2(e) and 2(f)). The initial circular gridlines experimental technique has not been properly addressed in previous known ECAE research [1–27].

The proposed complex of experimental techniques for physical simulation of SPD during ECAE in Figures 1 and 2 will find the further applications in the study of viscous ECAE through dies with more complex Iwahashi, Luis-Perez, Utyashev, conform and equal radii geometries and the investigation of equal channel multiple angular extrusion.

5. CFD-Based Phenomenological Approach

In order to derive the mathematical model of viscous material flow during ECAE through the 2θ angular dies AOC–BED with channel intersection angle $\angle(\text{BED}) = \angle(\text{AOC}) = 2\theta$ we will address the CFD concepts and techniques. The main computational approach of the present article is based on the Navier-Stokes equations introduction to polymeric material viscous ECAE flow through 2θ angular dies AOC–BED of Segal (Figures 1, 2, 3(a), 3(c), 4, 5, 6(a), 6(c), 7, 8, 9(a), 9(c), 10, 11, 12(a), 12(c), 13, 14, 15, 16, and 17) and Iwahashi (Figures 3(b), 3(d), 6(b), 6(d), 9(b), 9(d), 12(b), and 12(d)) geometries. To use both dimensional and dimensionless values, the dimensional values are marked with over-line symbols.

The theoretical background for the introduction of Navier-Stokes equations as the first rheological approach to polymer non-Newtonian flow has been outlined by Goodwin and Hughes (2008) in pp. 55–65 of [29]; Oswald (2009) in pp. 45–169 of [30]; Pethrick (2007) in pp. 75–79 of [31]; Rubinstein and Colby (2003) in pp. 309–318 of [32]; and Strobl (2007) in pp. 223–286 of [34]. The theoretical background for the use of the Navier-Stokes equations in the present article for ECAE through the 2θ angular dies AOC–BED is as follows. For the anomalous or non-Newtonian liquids the law of internal friction is defined by the Bingham equation as $\tau = \tau_0 + \eta_{\text{vis}} \cdot (dw/dz)$, where τ_0 is the tangential stress within the viscous fluid model at rest before the beginning of the ECAE process. The viscous liquid can flow only after overcoming the τ_0 tangential stresses. Then for $\tau > \tau_0$ we have that $\tau_S = \eta_{\text{vis}} \cdot (dw/dz)$, where $\tau_S = \tau - \tau_0$ is the degree to which the tangential stresses exceed the fluidity level. In
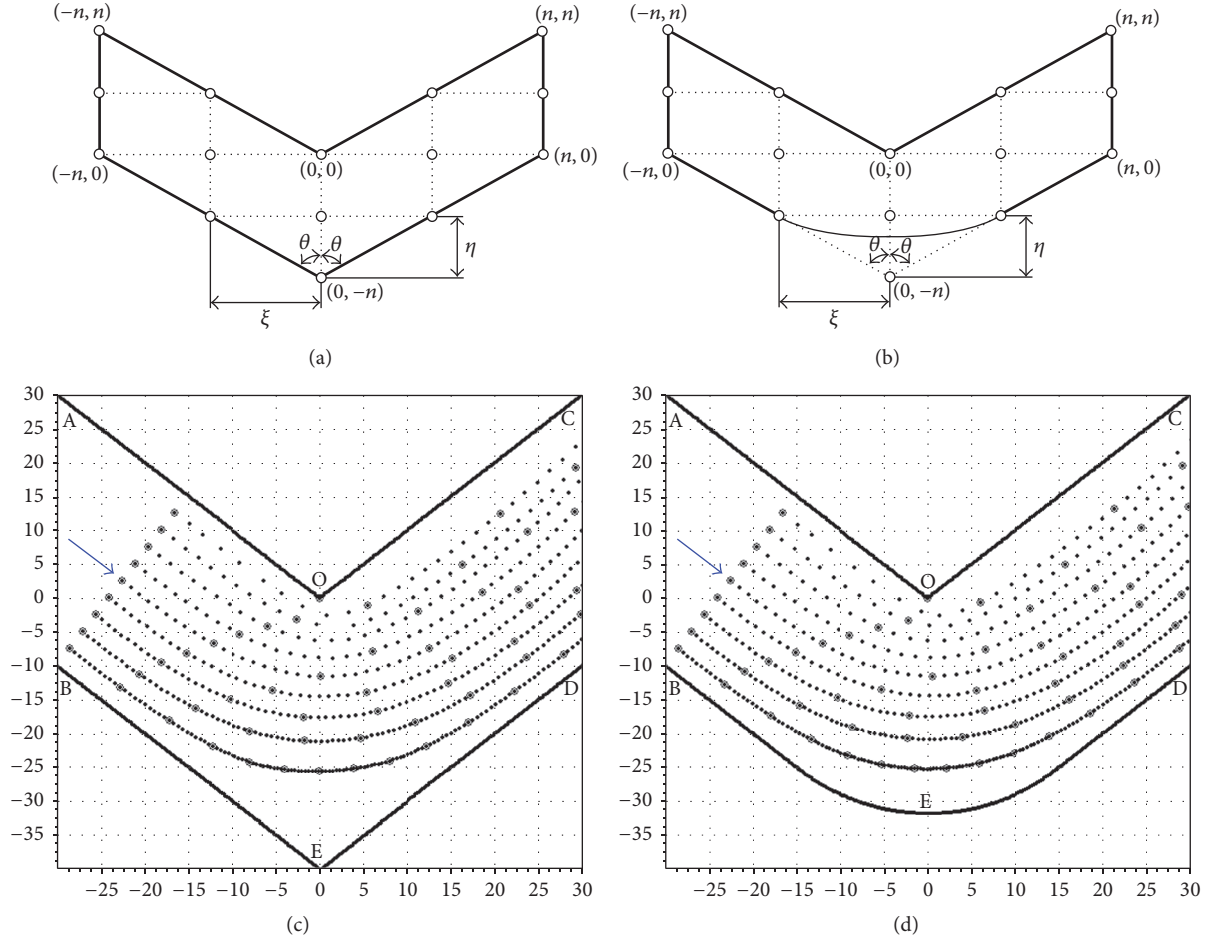
FIGURE 3: The finite difference meshes (a, b) and the computational flow lines (c, d) with dead zone formation (p. E) in vicinity of the external obtuse angle ∠(BED) (a, c) and for the "dead zone free" viscous flow (b, d) of a plasticine workpiece model through obtuse-angled equal channel angular dies AOC–BED of Segal (a, c) and Iwahashi geometries (b, d) with channel intersection angles ∠(AOC) = 2θ = 105° and external rounding BED in channel intersection zones R = 15 mm (b, d), where the time distance between small points of computational flow lines is 3 s, and the time distance between circles of computational flow lines is 30 s.

this work for ECAE viscous flow through the 2θ angular dies AOC–BED we deal with the steady flow regime of polymer workpiece models, when the fluidity level is overcome. So for the Bingham fluid we have the same Navier-Stokes equations as in the case of a Newtonian liquid, but the computational value of the tangential stress in reality is the overcoming of the tangential stress above the fluidity level. Taking into account all these considerations in the present article we are using the Navier-Stokes equations as the first ideal viscous approach to polymer flow through the 2θ angular dies of Segal and Iwahashi geometries during ECAE SPD forming.

The curl (vorticity) transfer equation is based on the Navier-Stokes equations [35]. The curl transfer equation in dimensionless variables will have the following form (Appendix A):

$$\frac{\partial \zeta}{\partial t} = -\text{Re}\left(\frac{\partial(u\zeta)}{\partial x} + \frac{\partial(v\zeta)}{\partial y}\right) + \left(\frac{\partial^2 \zeta}{\partial x^2} + \frac{\partial^2 \zeta}{\partial y^2}\right), \quad (1)$$

where the dimensionless curl (vorticity) function ζ (Figures 6(c), 6(d), 7(c), 7(d), 8(c), and 8(d)) will be defined as

$$\zeta = \frac{\partial u}{\partial y} - \frac{\partial v}{\partial x}. \quad (2)$$

The initial conditions for system (1)-(2) have no basic importance because we study mainly the stationary solution of system (1)-(2).

The numerical solution of the viscous flow problem for material flow in the 2θ angular ECAE die AOC–BED requires the formulation of a boundary value problem (Appendix A) for the Navier-Stokes equation in the curl (vorticity) transfer form (1)-(2) for $\partial \zeta/\partial t = -\text{Re}(\partial(u\zeta)/\partial x + \partial(v\zeta)/\partial y) + \partial^2 \zeta/\partial x^2 + \partial^2 \zeta/\partial y^2$, where $\zeta = \partial u/\partial y - \partial v/\partial x$ (Figures 6(c), 6(d), 7(c), 7(d), 8(c), and 8(d)). Equations (1)-(2) are written in finite-difference form for further numerical integration according to the method of alternating directions (Appendix A). In the finite difference form of (1)-(2) (Appendix A) we use upper indices (superscripts) near dimensionless functions ζ
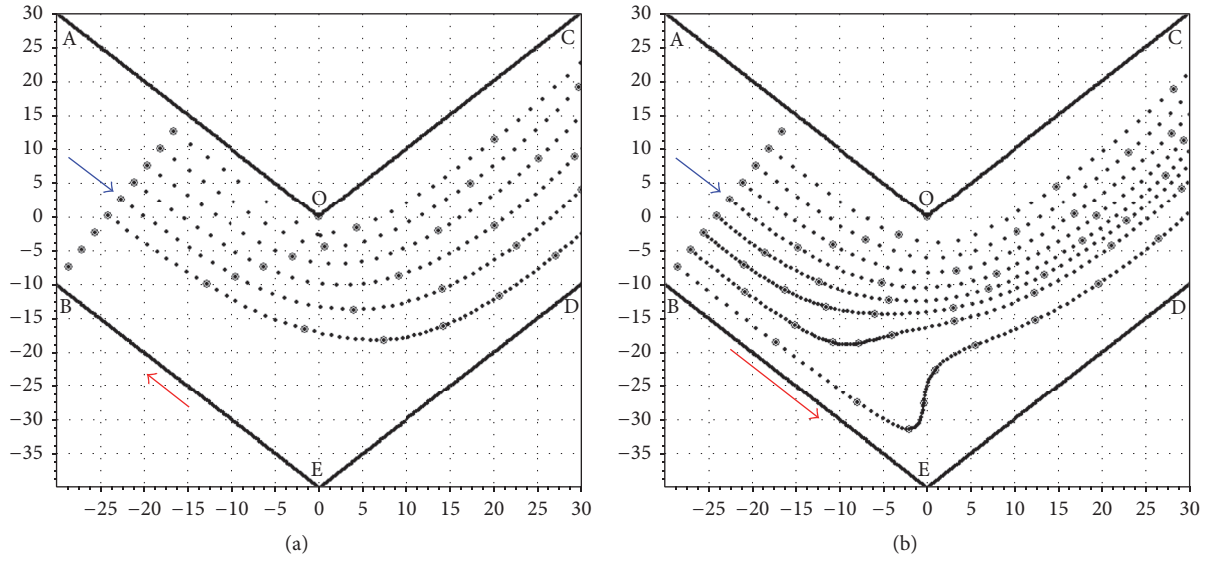
FIGURE 4: CFD-derived flow lines for a Segal die with channel intersection angles $\angle(AOC) = 2\theta = 105°$, where inlet die wall BE moves upstream towards the punching direction with velocity $V_w = -U_0$ (a), and inlet die wall BE moves downstream stream-wise with increased velocity $V_w = 2U_0$ (b), where U_0 is punching velocity and the dimensional transition times are 1258 ms = 1.258 s (a) and 1797 ms = 1.797 s (b).
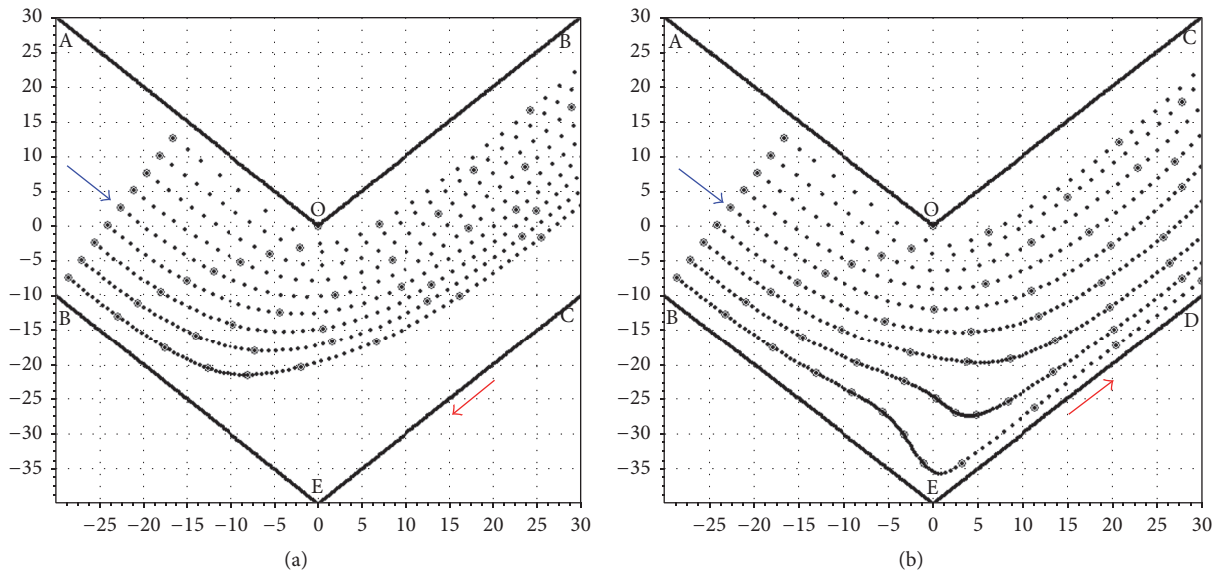

FIGURE 5: CFD-derived flow lines for a Segal die with channel intersection angles $\angle(AOC) = 2\theta = 105°$, where outlet die wall ED moves upstream towards the punching direction with velocity $V_w = -U_0$ (a), and outlet die wall ED moves downstream stream-wise with velocity $V_w = +U_0$ (b), where U_0 is punching velocity and the dimensional transition times are 1172 ms = 1.172 s (a) and 1831 ms = 1.831 s (b).

(Figures 6(c), 6(d), 7(c), 7(d), 8(c), and 8(d)), ψ (Figures 6(a), 6(b), 7(a), 7(b), 8(a), and 8(b)), u (Figures 9(a), 9(b), 10(a), 10(b), 11(a), and 11(b)), and v (Figures 9(c), 9(d), 10(c), 10(d), 11(c), and 11(d)) to denote the number of the time step. In the finite difference form of (1)-(2) (Appendix A) we will use lower indices (subscripts) near dimensionless functions ζ (Figures 6(c), 6(d), 7(c), 7(d), 8(c), and 8(d)), ψ (Figures 6(a), 6(b), 7(a), 7(b), 8(a), and 8(b)), u (Figures 9(a), 9(b),

10(a), 10(b), 11(a), and 11(b)), and v (Figures 9(c), 9(d), 10(c), 10(d), 11(c), and 11(d)) to denote cell numbers, where the first subscript will mark cell numbers along the dimensionless abscissa x (Figures 3–17) and the second subscript will mark cell numbers along the dimensionless ordinate y (Figures 3–17).

Flow (stream) function ψ (Figures 6(a), 6(b), 7(a), 7(b), 8(a), and 8(b)) was found with the Richardson iteration
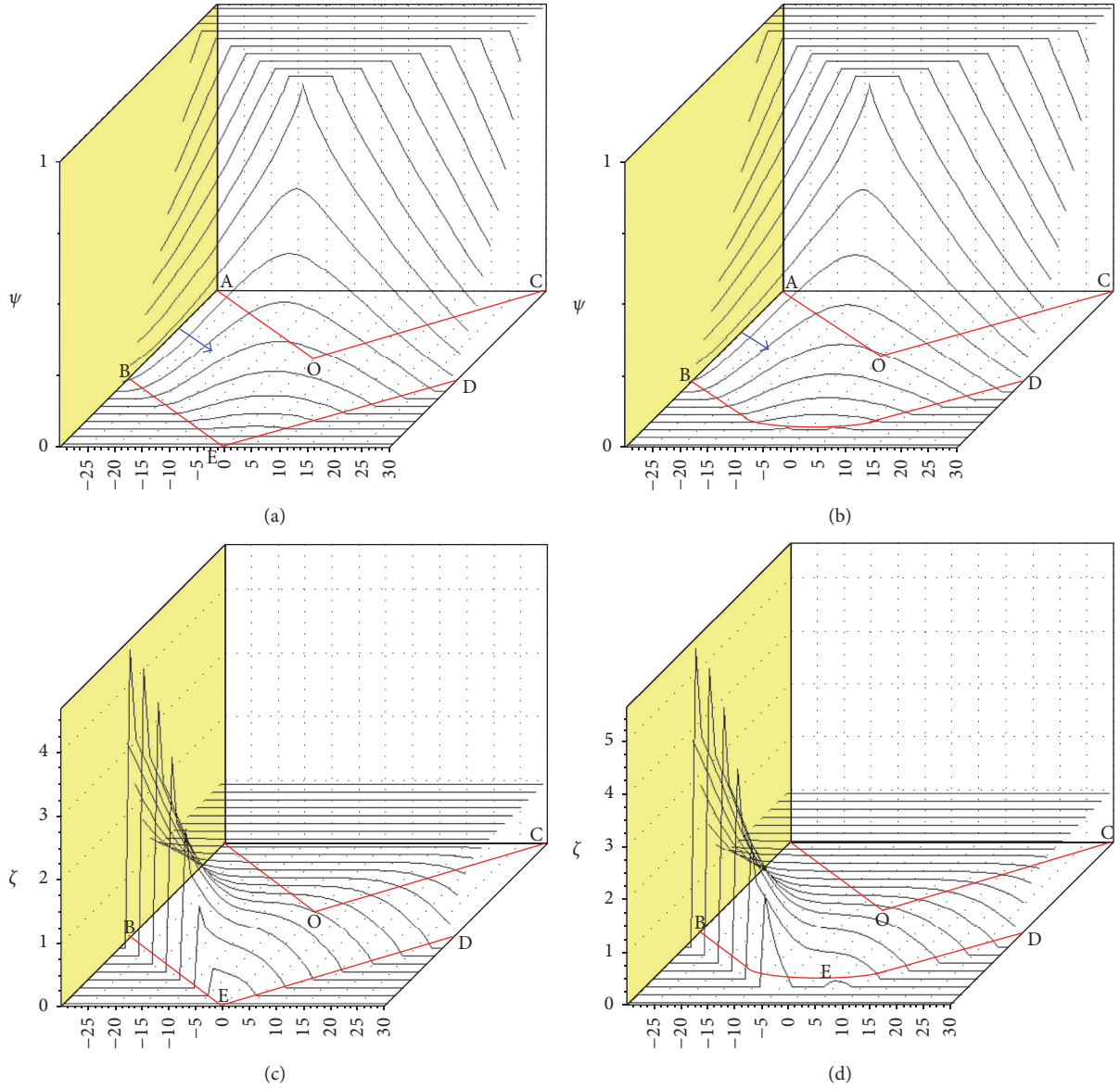
(a)

(b)

(c)

(d)

Figure 6: Computational diagrams for the dimensionless flow function ψ (a, b) and for the dimensionless curl function ζ (c, d) for the viscous flow of a plasticine workpiece model through obtuse-angled equal channel angular dies AOC–BED of Segal (a, c) and Iwahashi geometries (b, d) with channel intersection angles $\angle(AOC) = 2\theta = 105°$ and external rounding BED in channel intersection zones $R = 15$ mm (b, d), where the inlet AB is at the left and the outlet CD is at the right.

method. We now study the steady-state regime of the viscous flow (Figures 3–17) of a physical model of polymer material through the 2θ angular die AOC–BED. We assume initial conditions in the form of a rough approximation to the stationary solution. Unity initial values for ψ and ζ for the "upper region," which is located "higher" than left internal die wall (AOC), are in Figures 6–8:

$$\psi_{i,j}^0 = 1;$$
$$\zeta_{i,j}^0 = 1. \tag{3}$$

Initial values for ψ and ζ for the "lower region," which is located "lower" than the right external die wall (BED), are zero in Figures 6–8:

$$\psi_{i,j}^0 = 0;$$
$$\zeta_{i,j}^0 = 0. \tag{4}$$

Die channel wall boundary conditions (BCs) are defined as the sticking of viscous material to the die surface (Figures 3–17).
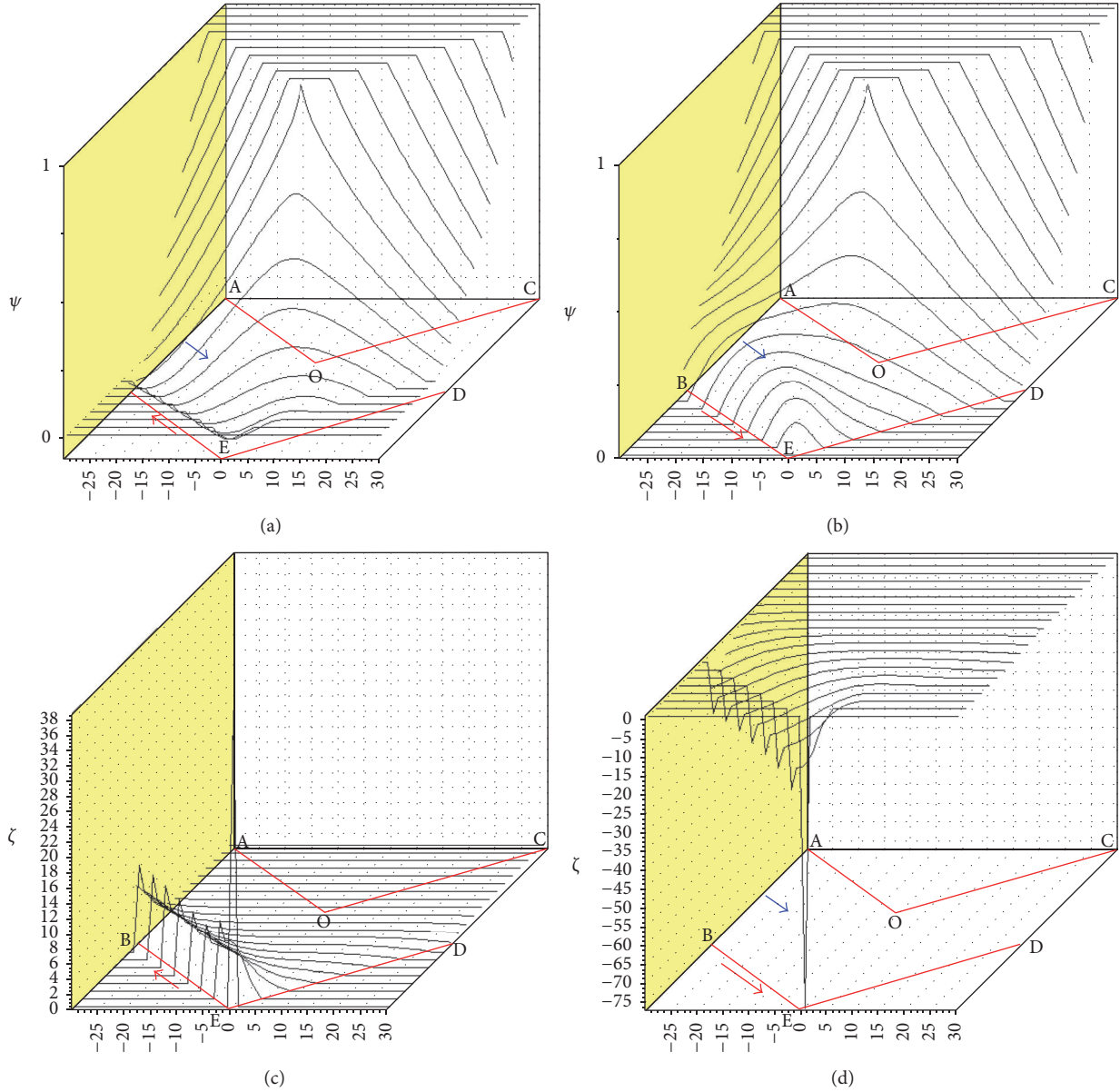
(a)

(b)

(c)

(d)

FIGURE 7: CFD-derived diagrams for the dimensionless flow function ψ (a, b) and for the dimensionless curl function ζ (c, d) for a Segal die with channel intersection angles $\angle(AOC) = 2\theta = 105°$, where inlet die wall BE moves upstream towards the punching direction with velocity $V_w = -U_0$ (a, c), inlet die wall BE moves downstream stream-wise with increased velocity $V_w = 2U_0$ (b, d), U_0 is punching velocity, and the dimensional transition times are 1.258 s (a, c) and 1.797 s (b, d).

For the right external die wall bound (BED) of the viscous flow in Figures 3–17 we have

$$\psi_{i,j} = 0;$$
$$\zeta_{i,j} = 0. \tag{5}$$

Boundary condition (5) for $\psi_{i,j} = 0$; $\zeta_{i,j} = 0$ occurs for $j \leq |i| - n$ (Figures 3–17).

For the left internal die wall bound (AOC) of viscous flow in Figures 3–17 we have

$$\psi_{i,j} = 1;$$
$$\zeta_{i,j} = 1. \tag{6}$$

Boundary condition (6) for $\psi_{i,j} = 1$; $\zeta_{i,j} = 1$ takes place for $j \geq |i|$ (Figures 3–17).

Figures 3, 6, 9, 12, and 13 provide the best illustration of BCs (5) and (6).

For the movable inlet die wall BE of the viscous flow with velocity V_w in Figures 4, 7, 10, 14, and 15, we have

$$u_{i,j} = V_w \sin\theta;$$

$$v_{i,j} = -V_w \cos\theta;$$

$$\zeta_{i,j}^{n+1} = \frac{2\left(\psi_{i+1,j+1}^{n+1} - V_w\sqrt{\eta^2 + \xi^2}\right)}{\eta^2 + \xi^2};$$
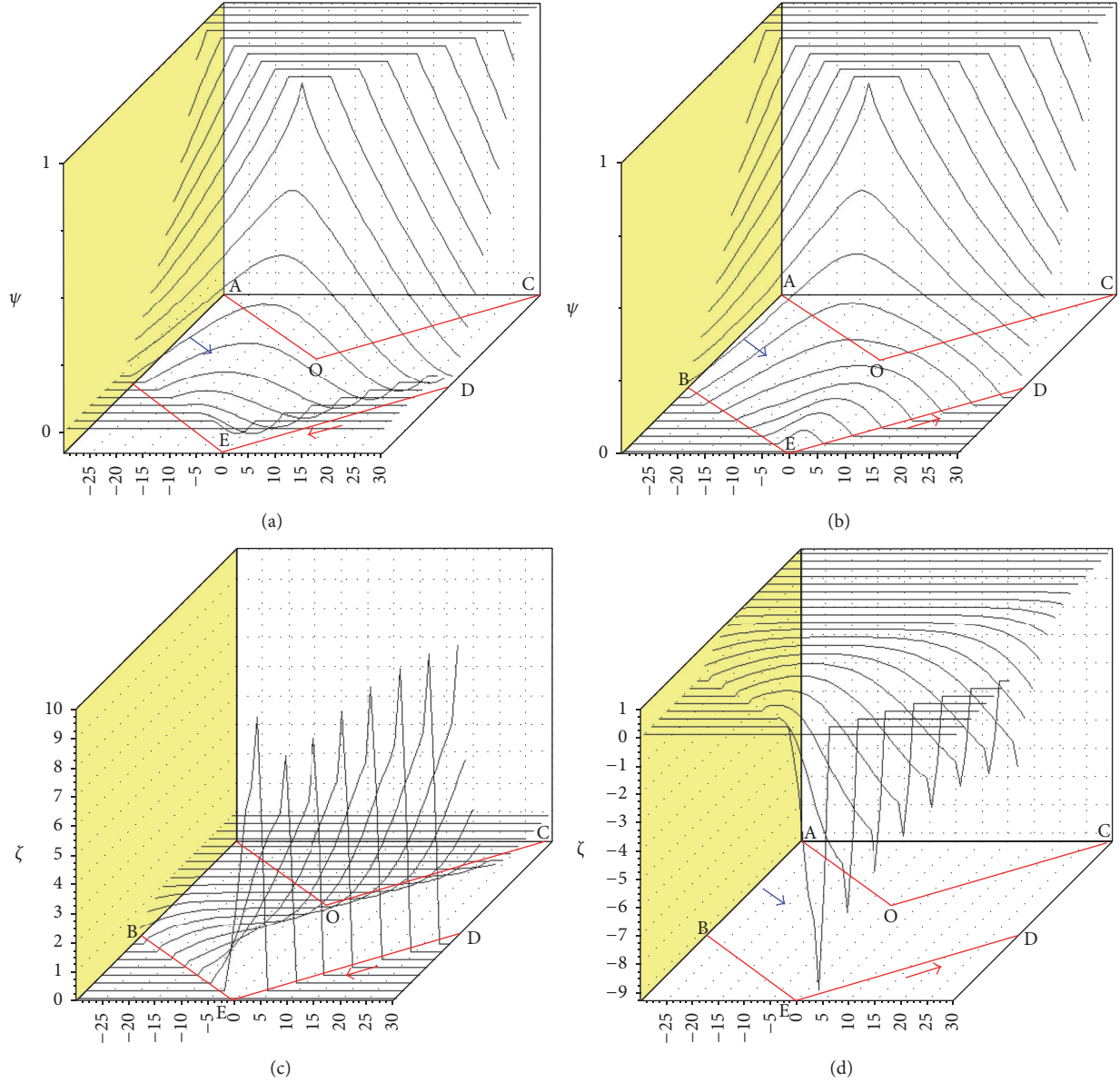
(a)

(b)

(c)

(d)

FIGURE 8: CFD-derived diagrams for the dimensionless flow function ψ (a, b) and for the dimensionless curl function ζ (c, d) for a Segal die with channel intersection angles $\angle(AOC) = 2\theta = 105°$, where outlet die wall ED moves upstream towards the punching direction with velocity $V_w = -U_0$ (a, c), outlet die wall ED moves downstream streamwise with velocity $V_w = +U_0$ (b, d), U_0 is punching velocity, and the dimensional transition times are 1172 ms = 1.172 s (a, c) and 1831 ms = 1.831 s (b, d).

$$\zeta_{i,j}^{n} = \frac{2\left(\psi_{i+1,j+1}^{n} - V_w \sqrt{\eta^2 + \xi^2}\right)}{\eta^2 + \xi^2},$$

$$(7)$$

where ξ and η are the horizontal and vertical coordinate steps along x- and y-axes, and the derivation of (7) is provided in Appendix B.

For the movable inlet die wall ED of the viscous flow with velocity V_w in Figures 5, 8, 11, 16, and 17 we have

$$u_{i,j} = V_w \sin\theta;$$

$$v_{i,j} = V_w \cos\theta;$$

$$\zeta_{i,j}^{n+1} = \frac{2\left(\psi_{i-1,j+1}^{n+1} - V_w \sqrt{\eta^2 + \xi^2}\right)}{\eta^2 + \xi^2};$$

$$\zeta_{i,j}^{n} = \frac{2\left(\psi_{i-1,j+1}^{n} - V_w \sqrt{\eta^2 + \xi^2}\right)}{\eta^2 + \xi^2},$$

$$(8)$$

where the derivation of (8) is provided in Appendix B.

The finite-difference form of the boundary value problem (1)–(8) is numerically solved by the method of successive iterations in Figures 3–17. Note that there is an influence
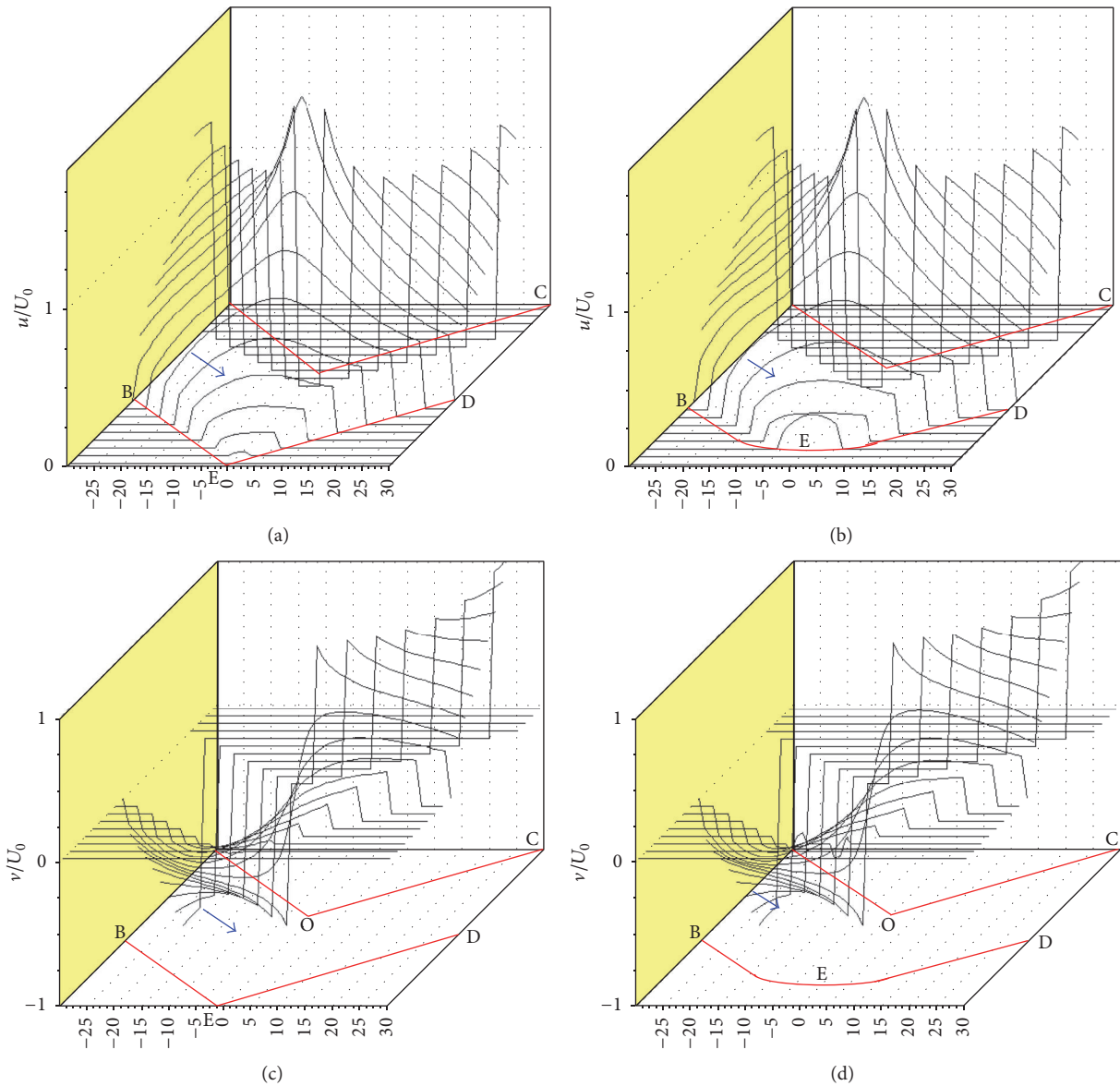
FIGURE 9: Computational diagrams for the dimensionless x-projection u of the flow velocity w (a, b) and for the dimensionless y-projection v of the flow velocity w (c, d) for the viscous flow of the plasticine workpiece model through obtuse-angled equal channel angular dies AOC–BED of Segal (a, c) and Iwahashi geometries (b, d) with channel intersection angles $\angle(AOC) = 2\theta = 105°$ and external rounding BED in channel intersection zones $R = 15$ mm (b, d), where the inlet AB is at the left and the outlet CD is at the right.

of instabilities of numerical solutions of the boundary value problem (1)–(8) at the entrance AB and at the exit CD of the viscous flow on the accuracy of the numerical integration results in Figures 3–17.

Instabilities of numerical finite-difference solutions of the boundary value problem (1)–(8), which appear at the inlet boundary AB (Figures 3–17) of the 2θ die AOC-BED, propagate in the punching direction along U_0, that is, moving downstream from AB to OE. Instabilities of numerical solutions of the boundary value problem (1)–(8), which appear at the outlet frontiers CD, move opposite the material flow direction, that is, propagating upstream from CD to OE.

The numerical solutions (Figures 3–17) for ECAE through the 2θ angular dies of Segal and Iwahashi geometries satisfactorily agree with the physical simulation results (Figures 1 and 2) only when the inlet boundary AB and outlet boundary CD of the viscous flows are located well away from studied zone OE of the channel intersection zone; that is, ideally the channel inlet AB and outlet CD are infinitely distant from the die channel intersection zone OE.

So in order to protect the numerical solutions (Figures 3–17) from numerical distortions, caused by instabilities at inlet zone AB, the distribution 2D and 3D plots of energy-power ECAE parameters in Figures 3–17 have been derived
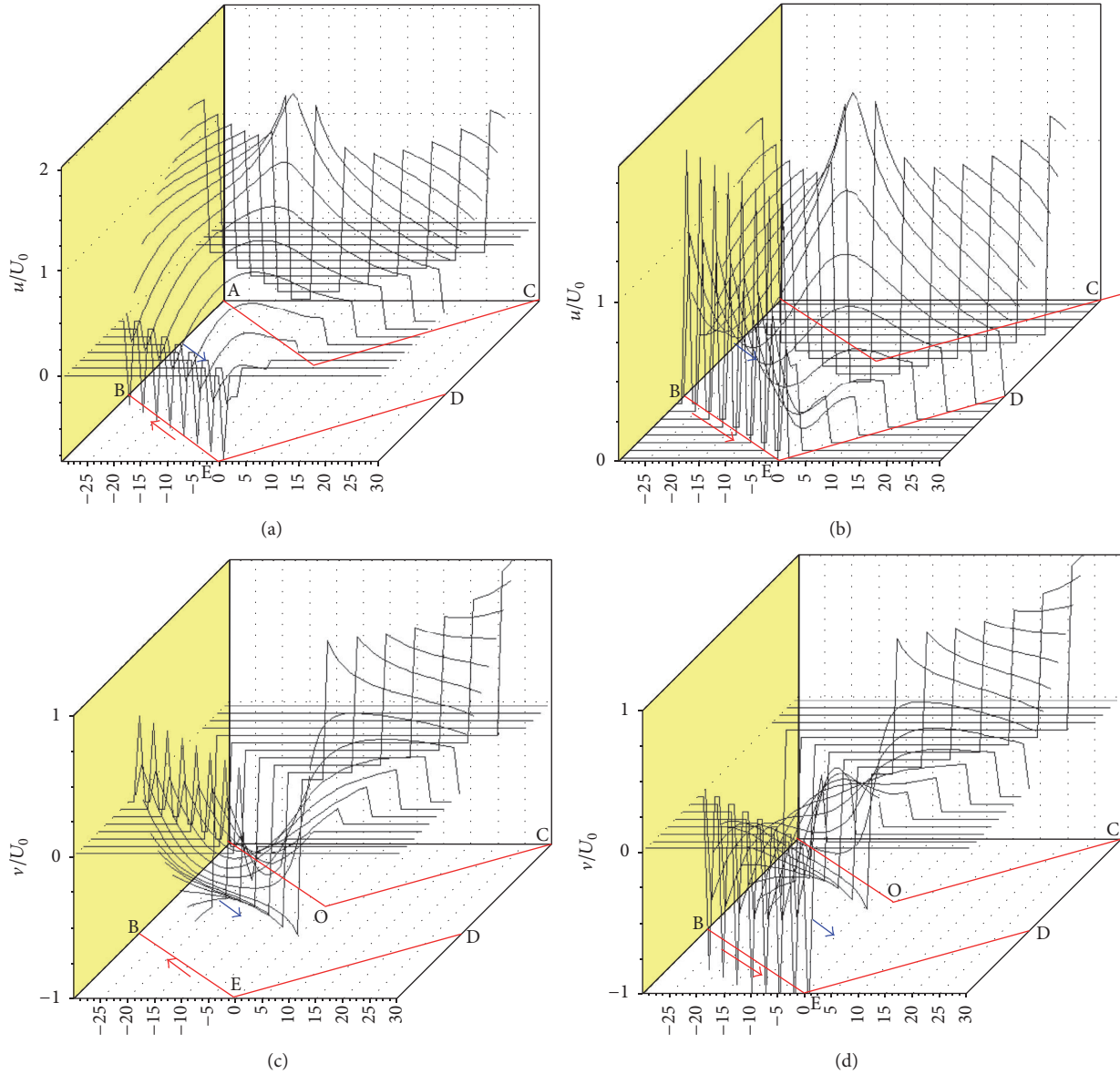
(a)

(b)

(c)

(d)

FIGURE 10: CFD-derived diagrams for the dimensionless x-projection u of the flow velocity w (a, b) and for the dimensionless y-projection v of the flow velocity w (c, d) for a Segal die with channel intersection angles $\angle(AOC) = 2\theta = 105°$, where inlet die wall BE moves upstream towards the punching direction with velocity $V_w = -U_0$ (a, c), inlet die wall BE moves downstream stream-wise with increased velocity $V_w = 2U_0$ (b, d), U_0 is punching velocity, and the dimensional transition times are 1.258 s (a, c) and 1.797 s (b, d).

assuming that the initial solution points are chosen not near coordinate grid inlet boundary AB of viscous flow but were chosen several cells away from the AB boundary.

Similarly for all 2D and 3D plots in Figures 3–17 the derived numerical fields have been truncated several cells away from the outlet CD finite-difference boundary in order to remove the computational distortions caused by the outlet CD instabilities. So the finite difference grid cells near the inlet AB and outlet CD have been rejected from the plots in Figures 3–17.

The numerical computation results of the CFD-based integration curl transfer equation (1)-(2) with the initial (3)-(4) and boundary (5)–(8) conditions for the fields of the flow lines (Figures 3(c), 3(d), 4, and 5) and energy-power

parameters (Figures 6–17) are outlined in Figures 3–17 for the following numerical values of physical variables:

die channel intersection angle is $2\theta = 105°$;

the dimensional width of inlet and outlet ECAE die channel is $\bar{a} = 15$ mm;

the dimensional external radius of the ECAE 2θ die of Iwahashi geometry is $\bar{R} = 15$ mm;

the dimensional density of the viscous plasticine physical model of extruded polymer material is $\bar{\rho} = 1850$ kg/m^3;

the dimensional plasticine yield strength is $\bar{\sigma}_s = 217$ kPa (Sofuoglu and Rasty (2000), [33]);

(a)

(b)

(c)

(d)

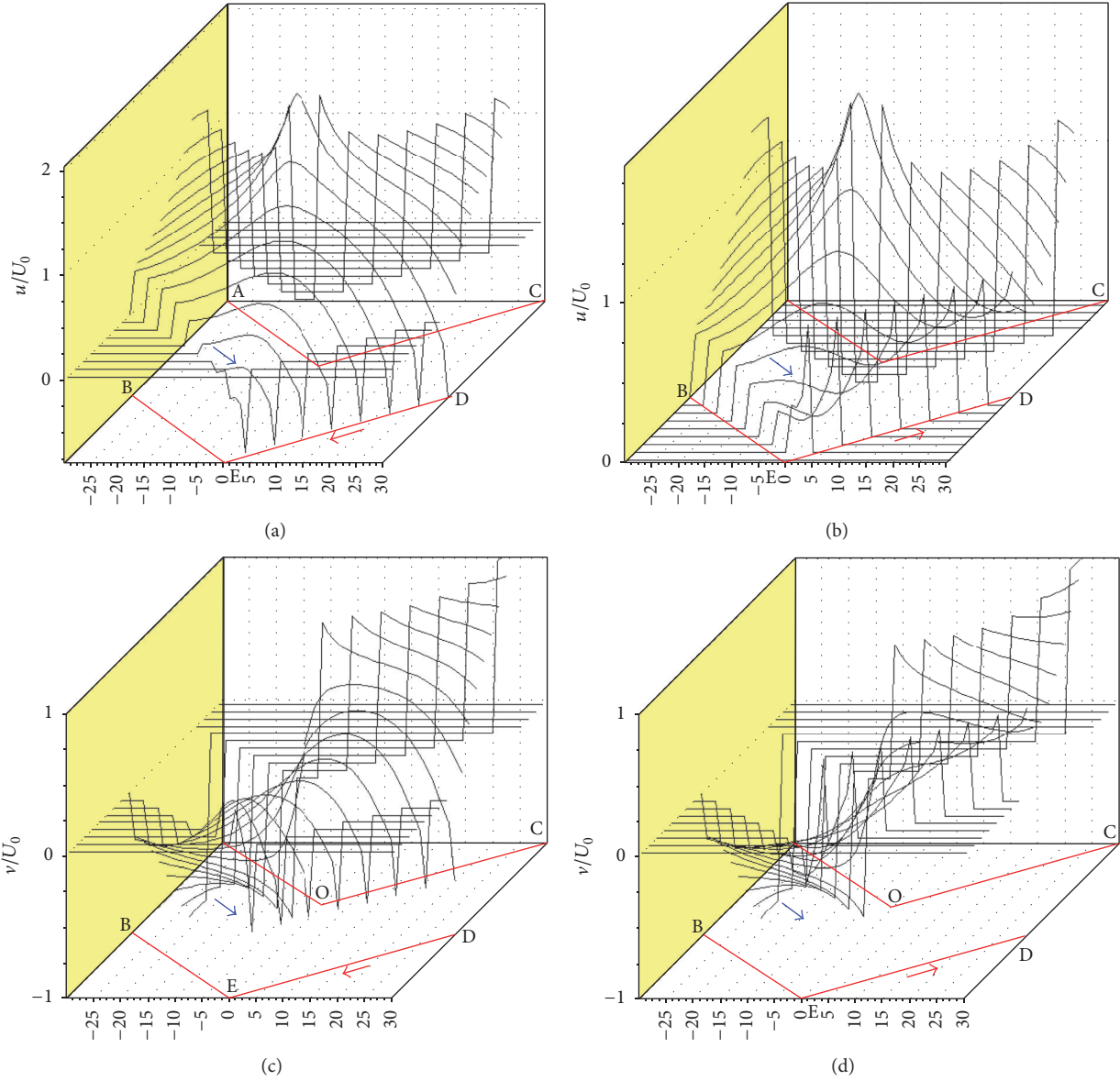FIGURE 11: CFD-derived diagrams for the dimensionless x-projection u of the flow velocity w (a, b) and for the dimensionless y-projection v of the flow velocity w (c, d) for a Segal die with channel intersection angles $\angle(AOC) = 2\theta = 105°$, where outlet die wall ED moves upstream towards the punching direction with velocity $V_w = -U_0$ (a, c), outlet die wall ED moves downstream stream-wise with velocity $V_w = +U_0$ (b, d), U_0 is punching velocity, and the dimensional transition times are 1172 ms = 1.172 s (a, c) and 1831 ms = 1.831 s (b, d).

the dimensional specific heat capacity of plasticine material is $\bar{c} = 1.004$ kJ/(kg·K);

the dimensional thermal conductivity is $\bar{\lambda} = 0.7$ J/(m·s·K) (Chijiiwa et al. (1981), [28]);

the dimensional dynamic viscosity for viscous Newtonian fluid model of the plasticine workpiece during ECAE is $\bar{\eta}_{vis} = 50$ Pa·s;

the dimensional kinematic viscosity for viscous Newtonian fluid model of the plasticine workpiece ECAE is $\bar{\nu}_{vis} = \bar{\eta}_{vis}/\bar{\rho} = 50/1850 \approx 0.027$ m^2/s;

the dimensional characteristic average ECAE punching velocity i.e. the workpiece velocity in the entrance

die channel (AOBE) is $\overline{U}_0 = 270\,\mu$m/s $= 0.27 \cdot 10^{-3}$ m/s;

the dimensionless Reynolds number is Re $= \overline{U}_0 \bar{a}\,\bar{\rho}/\bar{\eta}_{vis} = \overline{U}_0 \bar{a}/\bar{\nu}_{vis} = (0.27 \cdot 10^{-3} \cdot 15 \cdot 10^{-3})/0.027 = 1.50 \cdot 10^{-4}$;

the maximum value of dimensionless curl is $\zeta = 1$;

the dimensional curl is $\bar{\zeta} = \zeta \cdot \overline{U}_0/\bar{a} = (1 \cdot 0.27 \cdot 10^{-3}$ m/s$)/(15 \cdot 10^{-3}$ m$) = 18 \cdot 10^{-3}$ s^{-1};

the dimensional average angular velocity of rotation for processed viscous material elementary volume is $\bar{\omega} = |{\rm rot}\,\vec{w}|/2 = \bar{\zeta}/2 = 9 \cdot 10^{-3}$ s^{-1};
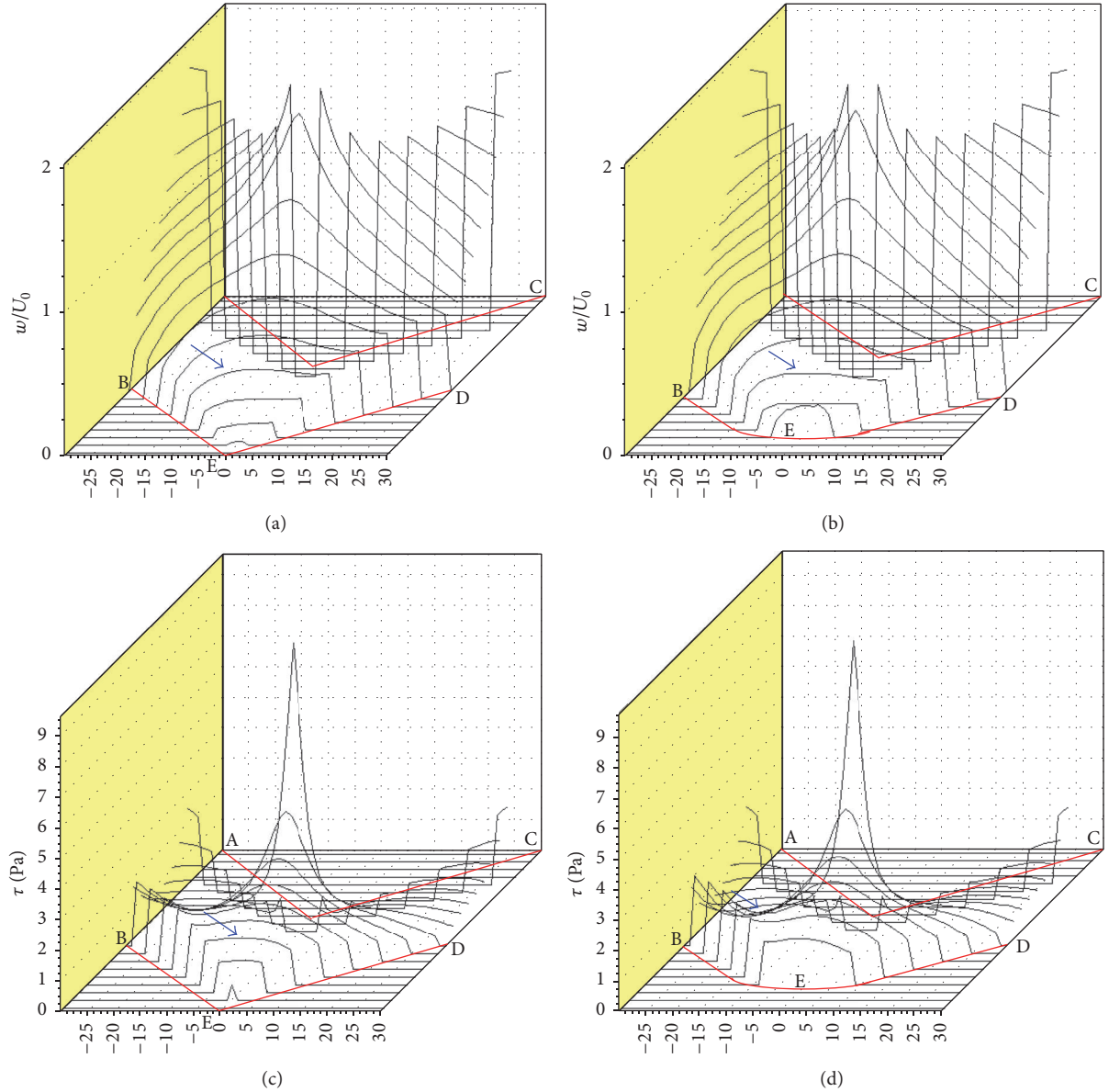
FIGURE 12: Computational 3D diagrams for dimensionless flow velocity w (a, b) and for dimensional tangential stress τ (c, d) for the viscous flow of a plasticine workpiece model through obtuse-angled equal channel angular dies AOC–BED of Segal (a, c) and Iwahashi geometries (b, d) with channel intersection angles $\angle(AOC) = 2\theta = 105°$ and external rounding BED in channel intersection zones $R = 15$ mm (b, d), where the inlet AB is at the left and the outlet CD is at the right.

the half number of coordinate steps along the x– and y– axes is $q = 40$;

the number of coordinate steps along the x– and y– axes is $2 \cdot q = 80$;

the horizontal coordinate step along the x-axis is $\bar{\xi} = 616\,\mu m = 6.16 \cdot 10^{-4}$ m;

the vertical coordinate step along y-axis is $\bar{\eta} = 473\,\mu m = 4.73 \cdot 10^{-4}$ m;

the dimensional time distance between small points of computational flow lines is 3 s;

the dimensional time distance between circles (i.e., between isochrones) of computational flow lines is 30 s;

the dimensional time iteration step is $\bar{t}_{it} = 2.69\,\mu s = 2.69 \cdot 10^{-6}$ s;

the dimensional transition time is 1204 ms = 1.204 s (Figures 3, 6, 9, 12, and 13);

the dimensional transition time is 1258 ms = 1.258 s (Figures 4(a), 7(a), 7(c), 10(a), 10(c), 14(a), 14(c), 15(c), and 15(d));
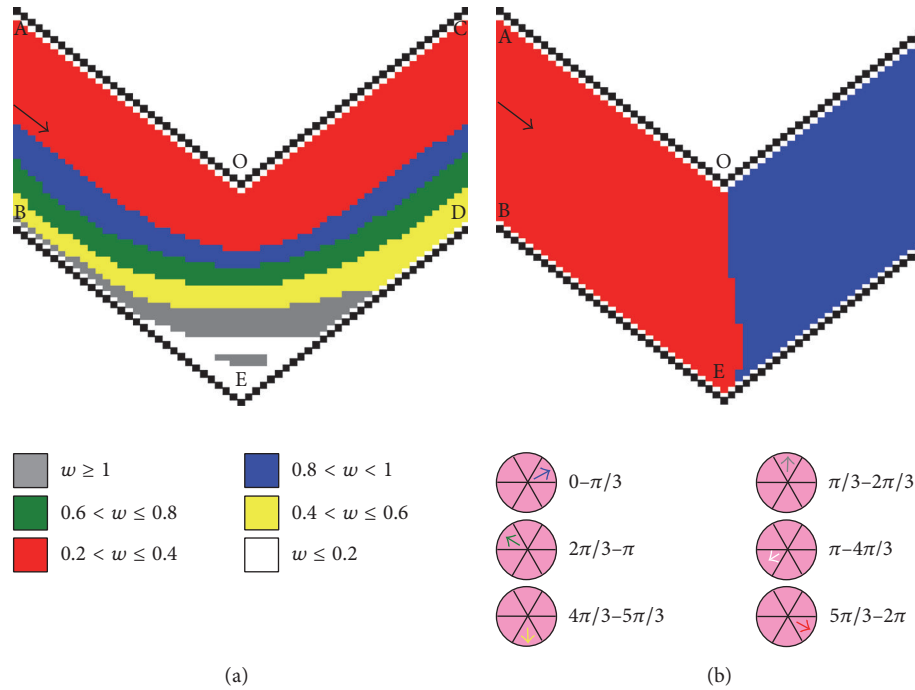
(a)

(b)

FIGURE 13: Computational 2D diagrams for the absolute value of dimensionless flow velocity w (a) and for directions of the vectors of dimensionless flow velocity $\mathbf{w}$ (b) for the viscous flow of a plasticine workpiece model through obtuse-angled equal channel angular dies AOC–BED of Segal geometry (a, b) with channel intersection angles $\angle(\text{AOC}) = 2\theta = 105$, where the inlet AB is at the left and the outlet CD is at the right.

the dimensional transition time is 1797 ms = 1.797 s (Figures 4(b), 7(b), 7(d), 10(b), 10(d), 14(b), 14(d), 15(a), and 15(b));

the dimensional transition time is 1172 ms = 1.172 s (Figures 5(a), 8(a), 8(c), 11(a), 11(c), 16(a), 16(c), 17(c), and 17(d));

the dimensional transition time is 1831 ms = 1.831 s (Figures 5(b), 8(b), 8(d), 11(b), 11(d), 16(b), 16(d), 17(a), and 17(b));

the dimensional ECAE punching pressure for the plasticine workpiece extrusion is $\overline{p} = 594$ kPa;

the relative error of iterations is $e = 1/1000$.

It is necessary to note that the 3D and 2D diagrams for the full flow dimensionless velocities w in Figures 12(a), 12(b), 13(a), 14(a), 14(b), 15(a), 15(c), 16(a), 16(b), 17(a), and 17(c) were derived on the basis of Figures 9, 10, and 11 for the dimensionless velocities' components u (Figures 9(a), 9(b), 10(a), 10(b), 11(a), and 11(b)) and v (Figures 9(c), 9(d), 10(c), 10(d), 11(c), and 11(d)) according to the formula for Pythagoras' theorem $w = (u^2 + v^2)^{0.5}$. The 3D diagrams for the dimensional tangential stresses in Figures 12(c), 12(d), 14(c), 14(d), 16(c), and 16(d) were derived on the basis of 3D diagrams of w in Figures 12(a), 12(b), 13(a), 14(a), 14(b), 15(a), 15(c), 16(a), 16(b), 17(a), and 17(c) according to Newtonian formula for viscous friction $\overline{\tau} = \overline{\eta}_{\text{vis}} \cdot |d\overline{w}/d\overline{z}|$.

So there is a direct correlation between the peak values in the 3D diagrams for dimensional tangential stresses in

Figures 12(c), 12(d), 14(c), 14(d), 16(c), and 16(d) and the maximum dimensionless flow velocities w in Figures 12(a), 12(b), 13(a), 14(a), 14(b), 15(a), 15(c), 16(a), 16(b), 17(a), and 17(c) because Figures 12(a), 12(b), 13(a), 14(a), 14(b), 15(a), 15(c), 16(a), 16(b), 17(a), and 17(c) are the spatial and planar plots of the flow velocities w functions, and Figures 12(c), 12(d), 14(c), 14(d), 16(c), and 16(d) are the spatial plots of the gradients dw/dz of the flow velocities w functions. The numerical solution of the boundary value problem (1)–(8) implicitly takes into account the maximum value of contact friction between the viscous amorphous polymer workpiece material and the walls of the ECAE 2θ die AOC-BED by the definition of full sticking during viscous fluid flow.

The computational flow lines in Figures 3(c), 3(d), 4, and 5 contain additional yellow bands between the successive isochrones. The time distance between the isochrones is 30 s. Additional yellow bands connect the points of the one isochrone for every moment of time. If it is assumed that workpiece viscous material sequentially fills the ECAE die AOC–BED, then the curved isochrones' lines show us the kinematics of viscous material flow for the every 30 s of the ECAE punching process through the ECAE die with $\angle(\text{BED}) = \angle(\text{AOC}) = 2\theta = 105°$.

Computational flow lines in Figures 3(c), 3(d), 4, and 5 for the viscous ECAE flow through the angular 2θ die AOC–BED of Segal geometry show us the formation of a symmetrical dead zone BED (p. E) in the vicinity of the external die angle $\angle(\text{BED}) = 2\theta = 105°$ at the right external border of the viscous flow, that is, on the external die wall BED in
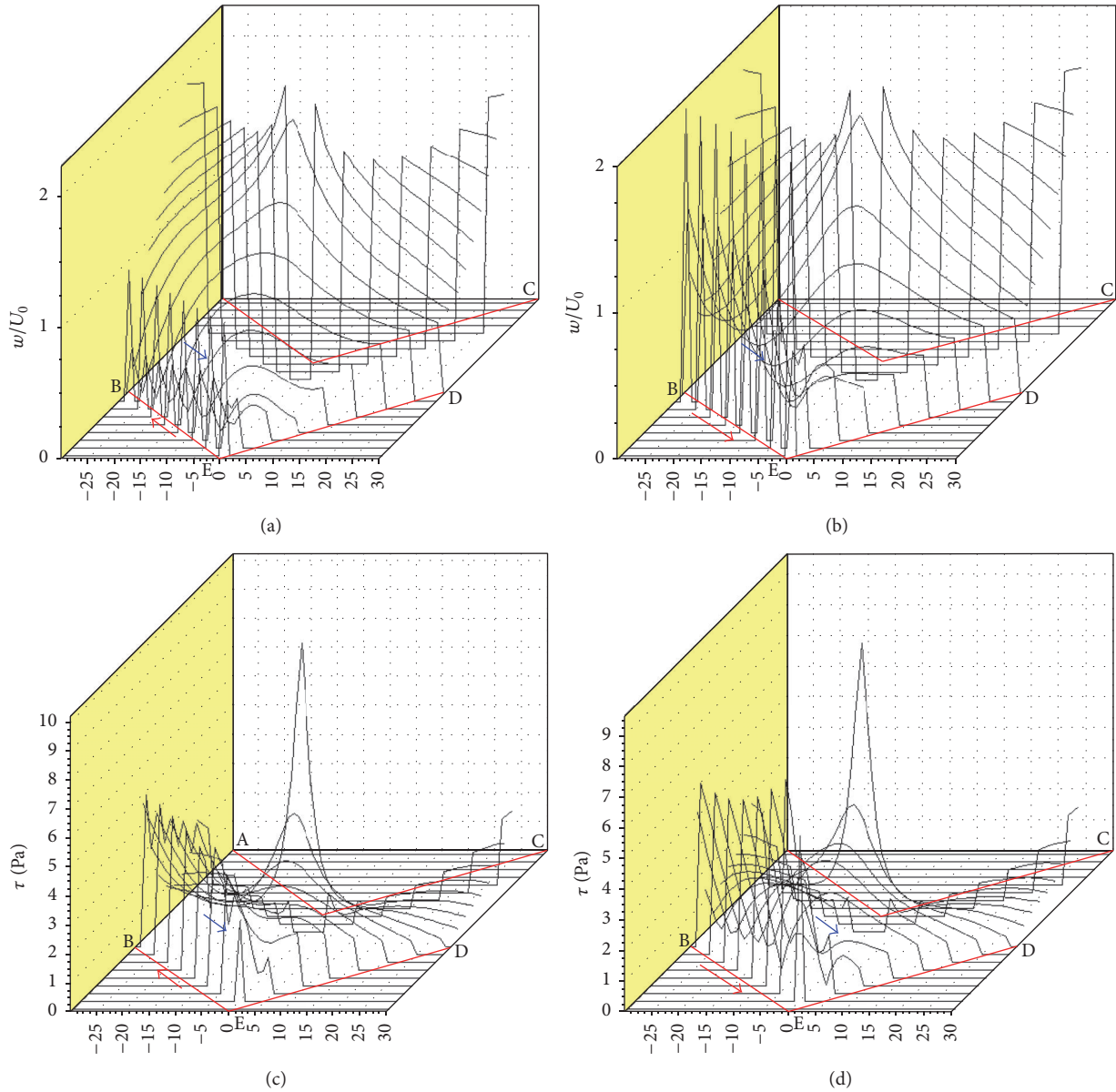
(a)

(b)

(c)

(d)

FIGURE 14: CFD-derived 3D diagrams for dimensionless flow velocity w (a, b) and for dimensional tangential stress τ (c, d) for a Segal die with channel intersection angles $\angle(AOC) = 2\theta = 105°$, where inlet die wall BE moves upstream towards the punching direction with velocity $V_w = -U_0$ (a, c), inlet die wall BE moves downstream stream-wise with increased velocity $V_w = 2U_0$ (b, d), U_0 is punching velocity, and the dimensional transition times are 1.258 s (a, c) and 1.797 s (b, d).

channel intersection zone EO. The computational flow lines in Figures 3(c), 3(d), 4, and 5 show us that the bisector line EO of the 2θ die is the symmetry axis for the dead zone BED. It is necessary to note that an assumption concerning the formation of an asymmetrical dead zone BED for ECAE of viscous incompressible continuum through a 2θ-die AOC– BED is completely unacceptable because possible asymmetry of dead zone BED (p. E) would result in a violation of viscous model incompressibility for the numerically solved boundary value problem (1)–(8).

This CFD-derived theoretical result about dead zone (p. E) formation in Figures 1, 2, 3(a), 3(c), 4, 5, 6(a), 6(c), 7,

8, 9(a), 9(c), 10, 11, 12(a), 12(c), 13, 14, 15, 16, and 17 is fully correlated with physical simulation-derived experimental results in Figures 1 and 2, which confirms the correctness of the proposed CFD-based computational approach to the finite-difference solution of the boundary value problem (1)– (8).

The computational results in Figures 3(b), 3(d), 6(b), 6(d), 9(b), 9(d), 12(b), and 12(d) for viscous ECAE flow through an angular 2θ die AOC–BED of Iwahashi geometry with external rounding BED in channel intersection zone OE show us the dead zone-free viscous flow of polymer workpiece model through the Iwahashi ECAE die with

FIGURE 15: Computational 2D diagrams for the absolute value of dimensionless flow velocity w (a, c) and for directions of the vectors of dimensionless flow velocity $\mathbf{w}$ (b, d) for the viscous flow of a plasticine workpiece model through obtuse-angled equal channel angular dies AOC–BED of Segal geometry (a, b) with channel intersection angles $\angle(AOC) = 2\theta = 105$, where inlet die wall BE moves upstream towards the punching direction with velocity $V_w = -U_0$ (c, d), inlet die wall BE moves downstream stream-wise with increased velocity $V_w = 2U_0$ (a, b), the inlet AB is at the left, and the outlet CD is at the right.

external radius. This CFD-derived theoretical result indicating absence of the dead zone at the right external border of the viscous flow BED is fully correlated with physical simulation-derived experimental results for Iwahashi dies.

6. Discussion

The proposed theoretical CFD-derived hydrodynamic analysis has shown that the correctness of numerical integration of the boundary value problem (1)–(8) and the accuracy of
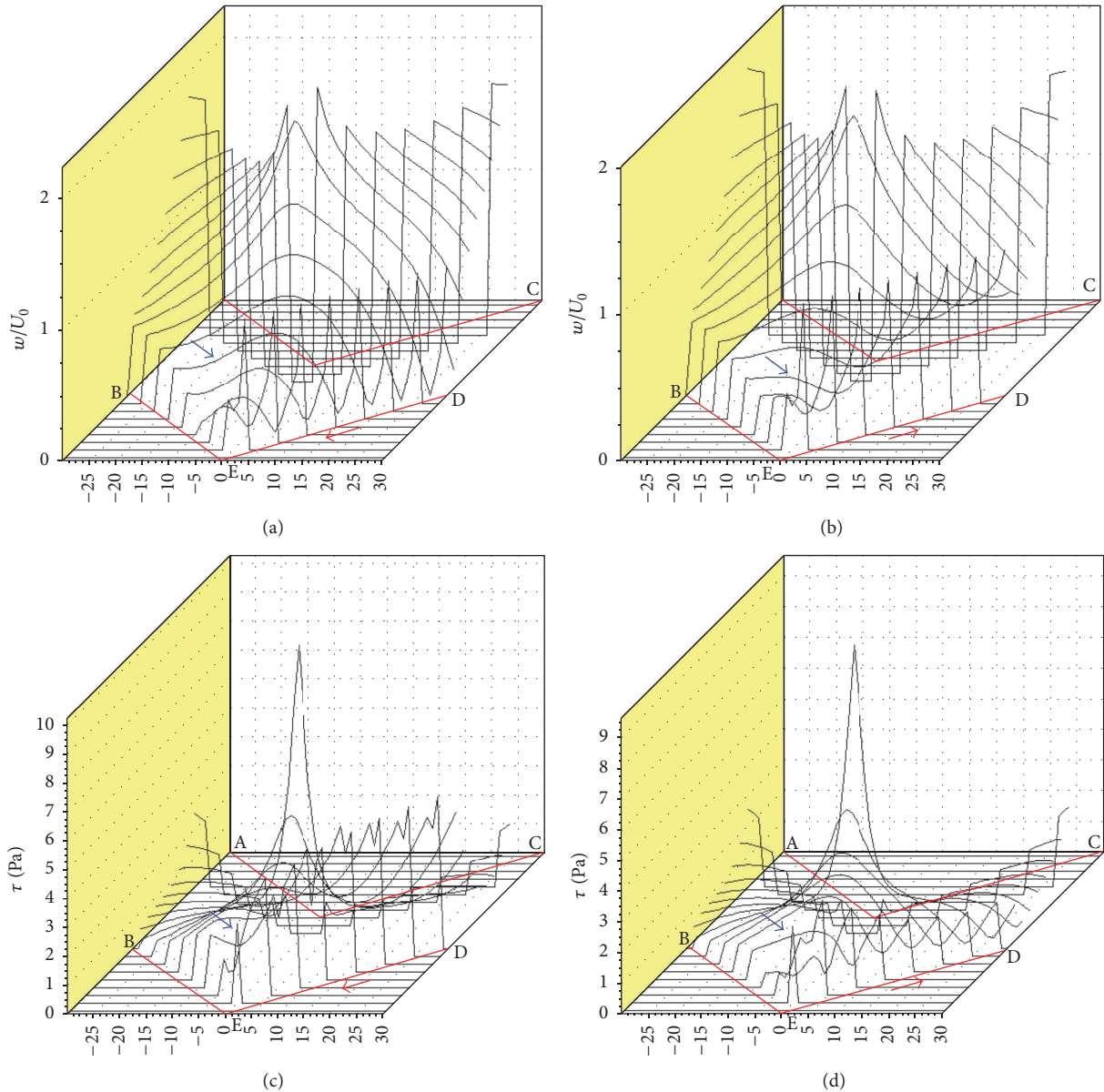
FIGURE 16: CFD-derived 3D diagrams for dimensionless flow velocity w (a, b) and for dimensional tangential stress τ (c, d) for a Segal die with channel intersection angles $\angle(AOC) = 2\theta = 105°$, where outlet die wall ED moves upstream towards the punching direction with velocity $V_w = -U_0$ (a, c), outlet die wall ED moves downstream streamwise with velocity $V_w = +U_0$ (b, d), U_0 is punching velocity, and the dimensional transition times are 1172 ms = 1.172 s (a, c) and 1831 ms = 1.831 s (b, d).

plane flow lines' plots and spatial diagrams of energy-power parameters for laminar Newtonian flows of the subject ECAE can be enhanced by the elimination of the influence of inlet AB and outlet CD numerical instabilities at the entrance ABOE and exit CDOE boundaries of viscous flow.

The peak values of computational dimensionless flow velocities $w = (u^2 + v^2)^{0.5}$ (Figures 12(a), 12(b), 13(a), 14(a), 14(b), 15(a), 15(c), 16(a), 16(b), 17(a), and 17(c)) and computational dimensional tangential stresses τ (Figures 12(c), 12(d), 14(c), 14(d), 16(c), and 16(d)) are located at the 2θ angle bisector line EO, that is, in the vicinity of channel intersection zone EO. So the CFD-derived diagrams for flow

velocities $w = (u^2 + v^2)^{0.5}$ (Figures 12(a), 12(b), 13(a), 14(a), 14(b), 15(a), 15(c), 16(a), 16(b), 17(a), and 17(c)) and tangential stresses τ (Figures 12(c), 12(d), 14(c), 14(d), 16(c), and 16(d)) additionally show that as the viscous workpiece model goes to the outlet channel OECD of the 2θ die AOC–BED of Segal geometry, the formation of velocity and tangential stress gradients occurs within the polymeric workpiece volume, adjacent to the line EO, and the localization of these gradients exactly corresponds to the die channel intersection zone EO.

At the mesomechanical level, the peaks of the computational values of $w = (u^2 + v^2)^{0.5}$ in Figures 12(a), 12(b), 13(a), 14(a), 14(b), 15(a), 15(c), 16(a), 16(b), 17(a), and 17(c) and τ in
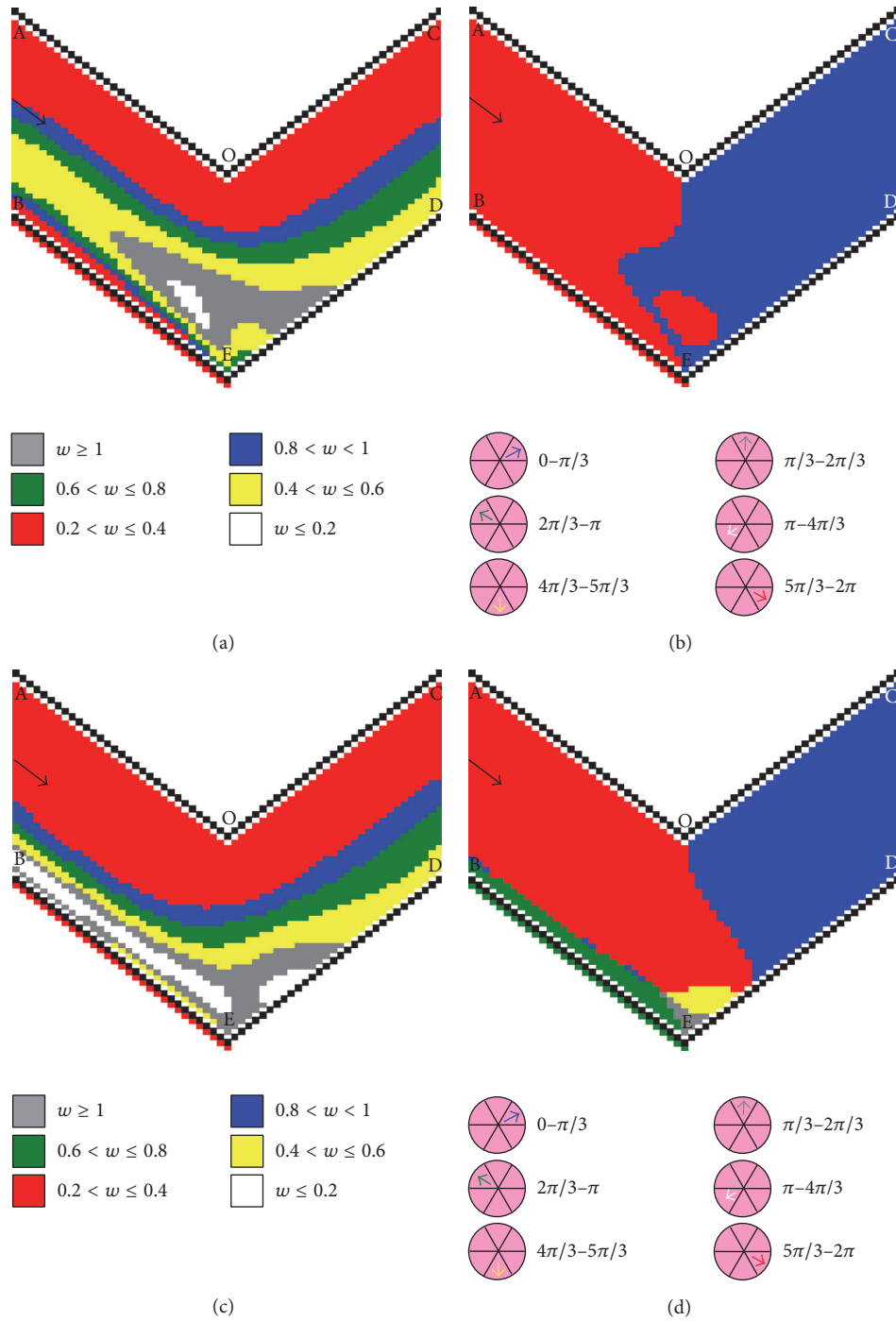
(a)

(b)

(c)

(d)
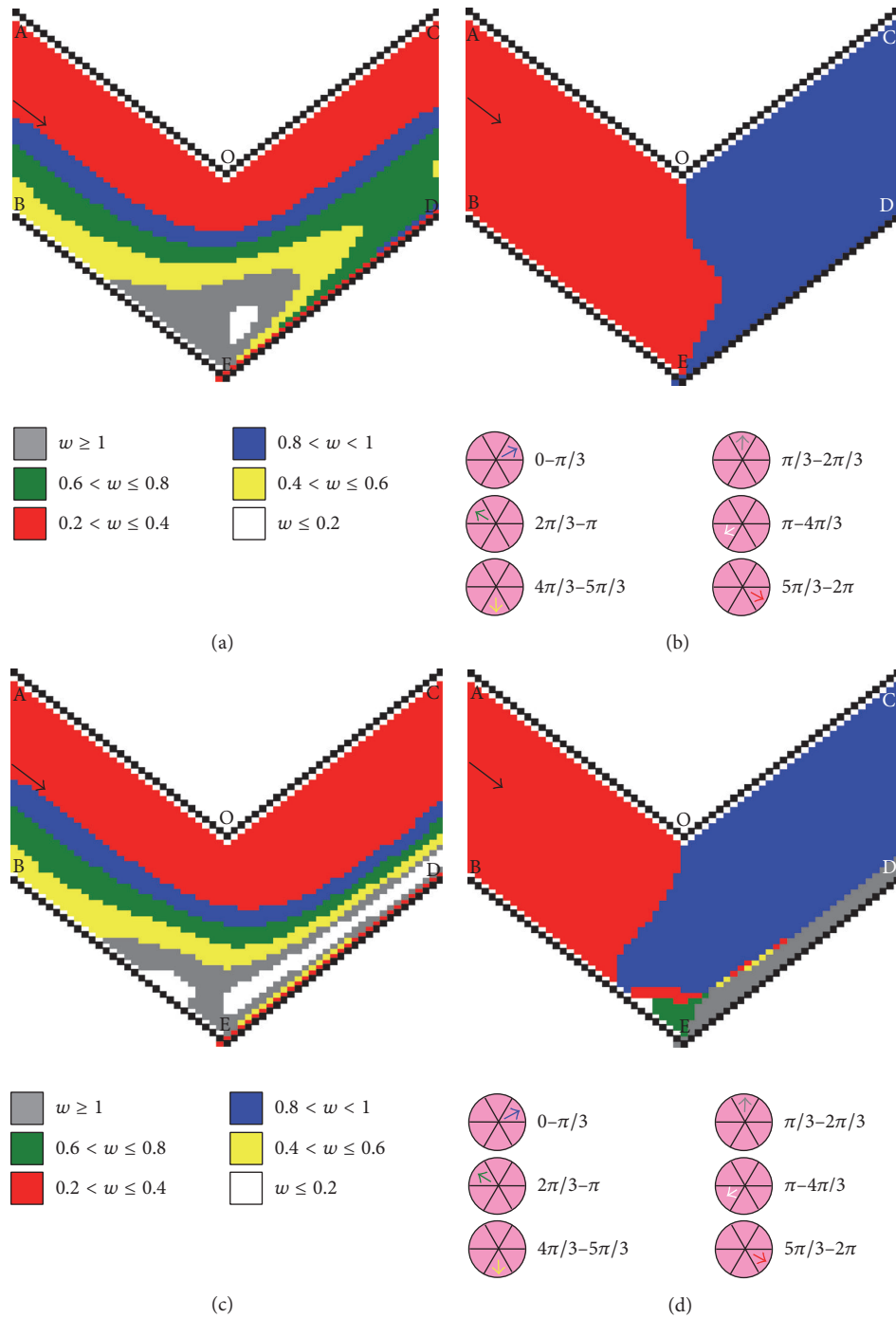
FIGURE 17: Computational 2D diagrams for the absolute value of dimensionless flow velocity w (a, c) and for directions of the vectors of dimensionless flow velocity **w** (b, d) for the viscous flow of a plasticine workpiece model through obtuse-angled equal channel angular dies AOC–BED of Segal geometry (a, b) with channel intersection angles $\angle(AOC) = 2\theta = 105$, where outlet die wall ED moves upstream towards the punching direction with velocity $V_w = -U_0$ (c, d), outlet die wall ED moves downstream stream-wise with velocity $V_w = +U_0$ (a, b), the inlet AB is at the left, and the outlet CD is at the right.

Figures 12(c), 12(d), 14(c), 14(d), 16(c), and 16(d) cause relative rotational motion of lamellae particles within the polymer workpiece continuum. As a result it causes the formation of rotary modes of SPD (Figures 1 and 2), accumulation of high strain unevenness in the volume of viscous material, and the localization of intensive macroscopic rotation within zone OECD of the outlet die channel CDOE (Figures 1–17) of the 2θ angular die AOC–BED during ECAE. So the computationally observable formation of tangential stress gradients on the CFD-derived diagrams in Figures 12(c), 12(d), 14(c), 14(d),

16(c), and 16(d) is the theoretical hydrodynamic illustration of the appearance of the rotational deformation modes, which are visually observable in the physical simulation-based experimental results, shown in Figures 1 and 2.

The combined use of the physical simulation (Figures 1 and 2) and numerical CFD techniques (Figures 3–17) provides new experimental-theoretical results, which illustrate the dynamics of local flow of viscous material during SPD with ECAE through the 2θ angular dies AOC–BED.

The proposed CFD-based approach (Figures 3–17) is simple, sound, and appropriate for the analysis of ECAE through the 2θ angled dies AOC–BED with more complex geometries like Iwahashi, Luis-Perez, Utyashev, and conform and equal radii geometries, taking into account the availability of the movable inlet and outlet die walls.

7. Conclusions

(1) With the introduction of an experimental physical simulation-based method of the initial circular colored gridlines in the shape of initial colorful cylindrical plasticine inclusions and a theoretical (numerical) finite-difference method, written for the boundary value problem (1)–(8) for Navier-Stokes equations in curl transfer form, we have achieved a complex experimental-theoretical description of the observable dynamics of macroscopic rotation formation within the volumes of viscous physical models of the subject ECAE.

(2) Physical simulation of macroscopic rotation in Figures 1 and 2 has been based on the proportionality of the values for viscous continuum rotation vector and the local angle for rotation of principal axes of viscous flow, that is, on the proportionality between material rotation vector and macroscopic rotation in the workpiece volume, visually observable with the introduction of the initial circular gridlines experimental technique. Numerical simulation of macroscopic rotation during flow of the continuum through the 2θ angular dies of Segal and Iwahashi geometries has been based on the proportionality of the values of full flow velocities in Figures 12(a), 12(b), 13(a), 14(a), 14(b), 15(a), 15(c), 16(a), 16(b), 17(a), and 17(c) and the gradients of flow velocities in Figures 12(c), 12(d), 14(c), 14(d), 16(c), and 16(d). The derived experimental-theoretical results allow the conclusion that the SPD ECAE forming of viscous polymer workpieces through the 2θ angular dies of Segal and Iwahashi geometries results in localization of the maximum tangential stresses within the workpiece worked material in the vicinity of channel intersection zone EO during ECAE. So the combined application of simulation techniques identified the formation of a dangerous zone, dangerous layers, and cross-sections for possible crack formation in viscous material flow within the polymeric workpiece material, which flows in the neighborhood of the 2θ angle bisector line EO, that is, in the vicinity of channel intersection zone EO of 2θ angular dies of Segal and Iwahashi geometries.

(3) A numerical hydrodynamic approach (Figures 3–17) to the analysis of viscous flow of amorphous viscous material during ECAE through a 2θ angular dies of Segal and Iwahashi geometries has been demonstrated, based on a numerical finite-difference solution of the boundary value problem (1)–(8) with the Navier-Stokes equations in curl transfer form. The corresponding numerical solution in Figures 3–17 accurately describes stationary two-dimensional flows of viscous incompressible Newtonian fluids in 2θ angular dies of Segal and Iwahashi geometries and also correctly accounts for the influence of inlet and outlet ECAE die channels.

(4) The derived experimental-theoretical results enhance the understanding of local viscous flow dynamics and the character of the formation of the rotational modes of deformations during Equal Channel Angle Extrusion through the 2θ angular dies of Segal and Iwahashi geometries and promises further application to the analysis of shear SPD flows in 2θ angular dies of more complex geometry with additional kinematic constraints in the shape of the moving walls.

Appendix

A. Boundary Value Problem Formulation

It is possible to write dimensional Navier-Stokes equations for x- and y-projections of dimensional velocities (Figures 9–17) and dimensional ECAE punching pressure in the following form [9, 13, 14, 17, 19, 20, 30, 35]:

$$
\frac{\partial \overline{u}}{\partial \overline{t}} + \overline{u}\frac{\partial \overline{u}}{\partial \overline{x}} + \overline{v}\frac{\partial \overline{u}}{\partial \overline{y}} = -\frac{1}{\rho} \cdot \frac{\partial \overline{p}}{\partial \overline{x}} + \overline{\nu}_{\text{vis}}
$$
$$
\cdot \left(\frac{\partial^2 \overline{u}}{\partial \overline{x}^2} + \frac{\partial^2 \overline{u}}{\partial \overline{y}^2} \right); \tag{A.1}
$$

$$
\frac{\partial \overline{v}}{\partial \overline{t}} + \overline{u}\frac{\partial \overline{v}}{\partial \overline{x}} + \overline{v}\frac{\partial \overline{v}}{\partial \overline{y}} = -\frac{1}{\rho} \cdot \frac{\partial \overline{p}}{\partial \overline{y}} + \overline{\nu}_{\text{vis}}
$$
$$
\cdot \left(\frac{\partial^2 \overline{v}}{\partial \overline{x}^2} + \frac{\partial^2 \overline{v}}{\partial \overline{y}^2} \right). \tag{A.2}
$$

It is convenient to mark with over-line symbols (i.e., with top underscores) the dimensional quantities in (A.1)-(A.2) and elsewhere. System (A.1)-(A.2) has two equations with three unknown functions: flow velocities $\overline{u}$ (Figures 9(a), 9(b), 10(a), 10(b), 11(a), and 11(b)), $\overline{v}$ (Figures 9(c), 9(d), 10(c), 10(d), 11(c), and 11(d)), and ECAE punching pressure $\overline{p}$. It is possible to close system (A.1)-(A.2) by adding the equation of continuity to the formulae (A.1)-(A.2):

$$
\frac{\partial \overline{u}}{\partial \overline{x}} + \frac{\partial \overline{v}}{\partial \overline{y}} = 0. \tag{A.3}
$$

It is necessary to derive the stationary solution of system (A.1)–(A.3) in Figures 3–17. Therefore the values of the initial conditions for system (A.1)–(A.3) have a little significance. It is necessary to do a further transformation of system (A.1)–(A.3) for the derivation of the numerical solution of the posed boundary value problem (A.1)–(A.3) in Figures 3–17. It is useful to introduce the curl (vorticity) transfer equation in order to solve only one partial derivative equation instead of system (A.1)–(A.3) of differential equations in partial derivatives. It is necessary to differentiate (A.1) with respect to

$\overline{y}$ and (A.2) with respect to $\overline{x}$. Then it is possible to eliminate ECAE punching pressure $\overline{p}$ and define the dimensional curl (vorticity) function $\overline{\zeta}$ (Figures 6(c), 6(d), 7(c), 7(d), 8(c), and 8(d)) as

$$\overline{\zeta} = \frac{\partial \overline{u}}{\partial \overline{y}} - \frac{\partial \overline{v}}{\partial \overline{x}}. \tag{A.4}$$

Therefore it is possible to get the following transfer partial derivative equation for dimensional curl (vorticity) function $\overline{\zeta}$ (Figures 6(c), 6(d), 7(c), 7(d), 8(c), and 8(d)):

$$\frac{\partial \overline{\zeta}}{\partial \overline{t}} = -\overline{u}\frac{\partial \overline{\zeta}}{\partial \overline{x}} - \overline{v}\frac{\partial \overline{\zeta}}{\partial \overline{y}} + \overline{v}_{\text{vis}} \cdot \left(\frac{\partial^2 \overline{\zeta}}{\partial \overline{x}^2} + \frac{\partial^2 \overline{\zeta}}{\partial \overline{y}^2} \right). \tag{A.5}$$

It is possible to reformulate the above-mentioned equation (A.5) in conservative form as

$$\frac{\partial \overline{\zeta}}{\partial \overline{t}} = -\frac{\partial \left(\overline{u}\overline{\zeta} \right)}{\partial \overline{x}} - \frac{\partial \left(\overline{v}\overline{\zeta} \right)}{\partial \overline{y}} + \overline{v}_{\text{vis}} \cdot \left(\frac{\partial^2 \overline{\zeta}}{\partial \overline{x}^2} + \frac{\partial^2 \overline{\zeta}}{\partial \overline{y}^2} \right). \tag{A.6}$$

It is important to note that the conservative form of (A.6) has implemented the integral conservation laws, which are valid for the original equations (A.1)–(A.3). It is possible to define the dimensional flow (stream) function $\overline{\psi}$ (Figures 6(a), 6(b), 7(a), 7(b), 8(a), and 8(b)) according to the following formulae:

$$\frac{\partial \overline{\psi}}{\partial \overline{y}} = \overline{u};$$
$$\frac{\partial \overline{\psi}}{\partial \overline{x}} = -\overline{v}. \tag{A.7}$$

It is possible to write (A.4) for the dimensional curl (vorticity) function $\overline{\zeta}$ (Figures 6(c), 6(d), 7(c), 7(d), 8(c), and 8(d)) in the following form:

$$\frac{\partial^2 \overline{\psi}}{\partial \overline{x}^2} + \frac{\partial^2 \overline{\psi}}{\partial \overline{y}^2} = \overline{\zeta}. \tag{A.8}$$

It is useful to introduce the following dimensionless variables: $u = \overline{u}/\overline{U}_0$; $v = \overline{v}/\overline{U}_0$; $x = \overline{x}/\overline{a}$; $y = \overline{y}/\overline{a}$; $\zeta = \overline{\zeta}\overline{a}/\overline{U}_0$; $\psi = \overline{\psi}/(\overline{U}_0\overline{a})$; $t = \overline{t}\overline{\eta}_{\text{vis}}/(\overline{\rho}\,\overline{a}^2)$; and $t = \overline{t}\overline{v}_{\text{vis}}/(\overline{a}^2)$. It is possible to write the curl (vorticity) transfer equation (A.6) in dimensionless variables in the following form:

$$\frac{\partial \zeta}{\partial t} = -\text{Re} \left(\frac{\partial (u\zeta)}{\partial x} + \frac{\partial (v\zeta)}{\partial y} \right) + \left(\frac{\partial^2 \zeta}{\partial x^2} + \frac{\partial^2 \zeta}{\partial y^2} \right). \tag{A.9}$$

It is possible to determine the dimensionless curl (vorticity) function ζ in (A.9) (Figures 6(c), 6(d), 7(c), 7(d), 8(c), and 8(d)) as

$$\zeta = \frac{\partial u}{\partial y} - \frac{\partial v}{\partial x}. \tag{A.10}$$

It is useful to introduce a finite-difference numerical technique for further numerical integration of the posed boundary value problem (A.9)-(A.10). The method of alternating directions for (A.9)-(A.10) yields the following finite-difference forms of (A.9)-(A.10) for the four cases of $\mathbf{i} \uparrow \mathbf{j} \uparrow$; $\mathbf{i} \downarrow \mathbf{j} \downarrow$; $\mathbf{i} \uparrow \mathbf{j} \downarrow$ and $\mathbf{i} \downarrow \mathbf{j} \uparrow$.

The case of $i \uparrow, j \uparrow$ produces

$$\zeta_{i,j}^{n+1} = \zeta_{i,j}^n - \text{Re}\tau \left(\left(\frac{u_{i+1,j}^n \zeta_{i+1,j}^n - u_{i-1,j}^n \zeta_{i-1,j}^n}{2\xi} \right) \right.$$
$$+ \left(\frac{v_{i,j+1}^n \zeta_{i,j+1}^n - v_{i,j-1}^n \zeta_{i,j-1}^n}{2\eta} \right) \right)$$
$$+ \left(\left(\frac{\zeta_{i+1,j}^n - \zeta_{i,j}^n + \zeta_{i-1,j}^{n+1}}{\xi^2} \right) \right.$$
$$\left. + \left(\frac{\zeta_{i,j+1}^n - \zeta_{i,j}^n + \zeta_{i,j-1}^{n+1}}{\eta^2} \right) \right) \tau. \tag{A.11}$$

The case of $i \downarrow, j \downarrow$ results in

$$\zeta_{i,j}^{n+1} = \zeta_{i,j}^n - \text{Re}\tau \left(\left(\frac{u_{i+1,j}^n \zeta_{i+1,j}^n - u_{i-1,j}^n \zeta_{i-1,j}^n}{2\xi} \right) \right.$$
$$+ \left(\frac{v_{i,j+1}^n \zeta_{i,j+1}^n - v_{i,j-1}^n \zeta_{i,j-1}^n}{2\eta} \right) \right)$$
$$+ \left(\left(\frac{\zeta_{i+1,j}^{n+1} - \zeta_{i,j}^n + \zeta_{i-1,j}^n}{\xi^2} \right) \right.$$
$$\left. + \left(\frac{\zeta_{i,j+1}^{n+1} - \zeta_{i,j}^n + \zeta_{i,j-1}^n}{\eta^2} \right) \right) \tau. \tag{A.12}$$

The case of $i \uparrow, j \downarrow$ yields

$$\zeta_{i,j}^{n+1} = \zeta_{i,j}^n - \text{Re}\tau \left(\left(\frac{u_{i+1,j}^n \zeta_{i+1,j}^n - u_{i-1,j}^n \zeta_{i-1,j}^n}{2\xi} \right) \right.$$
$$+ \left(\frac{v_{i,j+1}^n \zeta_{i,j+1}^n - v_{i,j-1}^n \zeta_{i,j-1}^n}{2\eta} \right) \right)$$
$$+ \left(\left(\frac{\zeta_{i+1,j}^n - \zeta_{i,j}^n + \zeta_{i-1,j}^{n+1}}{\xi^2} \right) \right.$$
$$\left. + \left(\frac{\zeta_{i,j+1}^{n+1} - \zeta_{i,j}^n + \zeta_{i,j-1}^n}{\eta^2} \right) \right) \tau. \tag{A.13}$$

The case of $i \downarrow, j \uparrow$ causes

$$\zeta_{i,j}^{n+1} = \zeta_{i,j}^n - \text{Re}\tau \left(\left(\frac{u_{i+1,j}^n \zeta_{i+1,j}^n - u_{i-1,j}^n \zeta_{i-1,j}^n}{2\xi} \right) \right.$$
$$+ \left(\frac{v_{i,j+1}^n \zeta_{i,j+1}^n - v_{i,j-1}^n \zeta_{i,j-1}^n}{2\eta} \right) \right)$$
$$+ \left(\left(\frac{\zeta_{i+1,j}^{n+1} - \zeta_{i,j}^n + \zeta_{i-1,j}^n}{\xi^2} \right) \right.$$
$$\left. + \left(\frac{\zeta_{i,j+1}^n - \zeta_{i,j}^n + \zeta_{i,j-1}^{n+1}}{\eta^2} \right) \right) \tau. \tag{A.14}$$

It is possible to determine a flow (stream) function ψ (Figures 6(a), 6(b), 7(a), 7(b), 8(a), and 8(b)) using Richardson iteration method with the following expression:

$$\psi_{i,j}^{k+1} = \frac{1}{2\left(1+\beta^2\right)}\left(\psi_{i+1,j}^k + \psi_{i-1,j}^k + \beta^2 \psi_{i,j+1}^k \right.$$
$$\left. + \beta^2 \psi_{i,j-1}^k - \xi^2 \zeta_{i,j}\right), \tag{A.15}$$

where $\beta = \xi/\eta$.

B. Formulation of Boundary Condition Expression for a Movable Die Wall

It is possible to expand of a flow (stream) function $\psi_{i,1}$ in Taylor series about point $(i, 0)$ of a movable die boundary, which moves with velocity u:

$$\psi_{i,1} = \psi_{i,0} + \left.\frac{\partial \psi}{\partial y}\right|_{i,0} \Delta y + \frac{1}{2}\left.\frac{\partial^2 \psi}{\partial y^2}\right|_{i,0} \Delta y^2$$
$$+ \frac{1}{6}\left.\frac{\partial^3 \psi}{\partial y^3}\right|_{i,0} \Delta y^3 + \cdots. \tag{B.1}$$

No-slip condition yields that

$$\left.\frac{\partial \psi}{\partial y}\right|_{i,0} = u. \tag{B.2}$$

It is possible to transform adhesion condition (B.2) to the form

$$\left.\frac{\partial^2 \psi}{\partial y^2}\right|_{i,0} = \left.\frac{\partial u}{\partial y}\right|_{i,0}. \tag{B.3}$$

It is possible to compute the value of right-hand side part of expression (B.3).

It is possible to simplify expression (2) for the dimensionless curl (vorticity) function ζ by taking into account that $v = 0$. So formula (2) after substitution $v = 0$ yields that

$$\zeta = \frac{\partial u}{\partial y} - \frac{\partial v}{\partial x} = \frac{\partial u}{\partial y}. \tag{B.4}$$

After substitution of (B.4) into (B.3) it is possible to get an expression for the right-hand side part of (B.3):

$$\left.\frac{\partial u}{\partial y}\right|_{i,0} = \zeta_{i,0}. \tag{B.5}$$

Substitution of (B.2) and (B.5) into (B.1) yields that

$$\psi_{i,1} = \psi_{i,0} + u\Delta y + \frac{1}{2}\zeta_{i,0}\Delta y^2 + \cdots. \tag{B.6}$$

The solution of equation (B.6) for $\zeta_{i,0}$ produces

$$\zeta_{i,0} \approx \frac{2\left(\psi_{i,1} - \psi_{i,0} - u\Delta y\right)}{\Delta y^2}. \tag{B.7}$$

Assuming that $\psi_{i,0} = 0$ one could get from (B.7) that

$$\zeta_{i,0} \approx \frac{2\left(\psi_{i,1} - u\Delta y\right)}{\Delta y^2}. \tag{B.8}$$

Derived expression (B.8) is used in this article for formulation of boundary conditions (7)-(8) for a movable die walls.

Nomenclature

SPD:	Severe Plastic Deformation
ECAE(P):	Equal Channel Angular Extrusion (Pressing)
CFD:	Computational Fluid Dynamics
BVP:	Boundary value problem
BC:	Boundary condition
2θ die:	Angular die AOC–BED with channel intersection angle $\angle(\text{BED}) = \angle(\text{AOC}) = 2\theta$ (Figures 1–17)
2θ die of Segal geometry:	Angular die AOC–BED with channel intersection angle $\angle(\text{BED}) = \angle(\text{AOC}) = 2\theta$ without external and internal radii in channel intersection zone (Figures 1, 2, 3(a), 3(c), 4, 5, 6(a), 6(c), 7, 8, 9(a), 9(c), 10, 11, 12(a), 12(c), 13, 14, 15, 16, and 17)
2θ die of Iwahashi geometry:	Angular die AOC–BED with channel intersection angle $\angle(\text{BED}) = \angle(\text{AOC}) = 2\theta$ and with external rounding in channel intersection zone (Figures 3(b), 3(d), 6(b), 6(d), 9(b), 9(d), 12(b), and 12(d))
$a; \overline{a}$:	Channel width of the ECAE 2θ die, [m]
$R; \overline{R}$:	External radius of the ECAE 2θ die of Iwahashi geometry, [m] (Figures 3(b), 3(d), 6(b), 6(d), 9(b), 9(d), 12(b), and 12(d))
Re:	Reynolds number of viscous workpiece model (given more fully in the paper)
$U_0; \overline{U}_0$:	Characteristic punching velocity of ECAE forming, [m/s]
$V_w; \overline{V}_w$:	Velocities of inlet and outlet external die walls BE and ED, [m/s]
$u; \overline{u}$:	x-projection of velocity of the point of viscous continuum, [m/s], where $u = \overline{u}/\overline{U}_0$
$v; \overline{v}$:	y-projection of velocity of the point of viscous continuum, [m/s], where $v = \overline{v}/\overline{U}_0$
$x; y; \overline{x}; \overline{y}$:	Cartesian rectangular coordinates of the points of viscous continuum, [m], where $x = \overline{x}/\overline{a}$; $y = \overline{y}/\overline{a}$ or $x = \text{Re} \cdot ut$; $y = \text{Re} \cdot vt$

$\zeta; \overline{\zeta}$:	Curl (vorticity) function for viscous continuum, [1/s], where $\zeta = \overline{\zeta}\overline{a}/\overline{U}_0$
$\overline{\nu}_{\text{vis}}$:	Kinematic viscosity of viscous workpiece model, [m^2/s]
$\overline{\eta}_{\text{vis}} = \overline{\nu}_{\text{vis}} \cdot \overline{\rho}$:	Dynamic viscosity of viscous workpiece model, [Pa·s]
$\overline{\rho}$:	Density of viscous physical model of polymer material, [kg/m^3]
$\psi; \overline{\psi}$:	Flow (stream) function for viscous continuum, [m^2/s], where $\psi = \overline{\psi}/(\overline{U}_0\overline{a})$
$p; \overline{p}$:	ECAE punching pressure, [Pa], where $p = \overline{p}/(\overline{\rho}\overline{U}_0^2)$
$\tau; \overline{\tau}$:	Tangential stress, [Pa];
$t; \overline{t}$:	ECAE time, [s], where $t = \overline{t}\overline{\eta}_{\text{vis}}/(\overline{\rho}\overline{a}^2)$ or $t = \overline{t}\overline{\nu}_{\text{vis}}/(\overline{a}^2)$
$\text{Re} = \overline{U}_0\overline{a}\,\overline{\rho}/\overline{\eta}_{\text{vis}}$:	Reynolds number of viscous continuum
N:	Quantity of ordinate steps along the channel width
$\xi; \overline{\xi}$:	Horizontal coordinate step along x-axis
$\eta; \overline{\eta}$:	Vertical coordinate step along y-axis
$t_{\text{it}}; \overline{t}_{\text{it}}$:	Time iteration step, [s]
k:	Iteration number
n:	Number of time step (in finite-difference formulae)
$i; j$:	Numbers of difference grid cells, where i corresponds to x-axis, and j corresponds to y-axis.

Additional Points

Highlights. Initial circular gridlines were applied to ECAE flow through 2θ Segal angular dies. BVP was posed and numerically solved for viscous flow through Segal and Iwahashi 2θ dies. The effect of fixed and movable inlet and outlet die walls was studied and analyzed during ECAE.

Disclosure

The submission of the authors' paper implies that it has not been previously published, that it is not under consideration for publication elsewhere, and that it will not be published elsewhere in the same form without the written permission of the editors.

Competing Interests

The authors Alexander V. Perig and Nikolai N. Golodenko declare that there is no conflict of interests regarding the publication of this paper.

Authors' Contributions

All authors participated in the design of this work and performed equally. All authors read and approved the final manuscript.

References

[1] B. Aour, F. Zaïri, R. Boulahia, M. Naït-Abdelaziz, J. M. Gloaguen, and J. M. Lefebvre, "Experimental and numerical study of ECAE deformation of polyolefins," *Computational Materials Science*, vol. 45, no. 3, pp. 646–652, 2009.

[2] V. A. Beloshenko, Y. V. Voznyak, I. Y. Reshidova, M. Naït-Abdelaziz, and F. Zairi, "Equal-channel angular extrusion of polymers," *Journal of Polymer Research*, vol. 20, no. 12, article no. 322, 2013.

[3] R. Boulahia, J. M. Gloaguen, F. Zaïri et al., "Deformation behaviour and mechanical properties of polypropylene processed by equal channel angular extrusion: effects of back-pressure and extrusion velocity," *Polymer*, vol. 50, no. 23, pp. 5508–5517, 2009.

[4] T. S. Creasy and Y. S. Kang, "Fiber orientation during equal channel angular extrusion of short fiber reinforced thermoplastics," *Journal of Thermoplastic Composite Materials*, vol. 17, no. 3, pp. 205–227, 2004.

[5] W. Z. Han, Z. F. Zhang, S. D. Wu, and S. X. Li, "Investigation on the geometrical aspect of deformation during equal-channel angular pressing by in-situ physical modeling experiments," *Materials Science and Engineering: A*, vol. 476, no. 1-2, pp. 224–229, 2008.

[6] A. M. Laptev, A. V. Perig, and O. Y. Vyal, "Analysis of equal channel angular extrusion by upper bound method and rigid blocks model," *Materials Research*, vol. 17, no. 2, pp. 359–366, 2014.

[7] H. Li, X. Huang, C. Huang, and Y. Zhao, "An investigation about solid equal channel angular extrusion on polypropylene/organic montmorillonite composite," *Journal of Applied Polymer Science*, vol. 123, no. 4, pp. 2222–2227, 2012.

[8] P. Minakowski, "Fluid model of crystal plasticity: numerical simulations of 2-turn equal channel angular extrusion," *Technische Mechanik*, vol. 34, no. 3-4, pp. 213–221, 2014.

[9] A. V. Perig, A. M. Laptev, N. N. Golodenko, Y. A. Erfort, and E. A. Bondarenko, "Equal channel angular extrusion of soft solids," *Materials Science and Engineering A*, vol. 527, no. 16-17, pp. 3769–3776, 2010.

[10] A. V. Perig, I. G. Zhbankov, and V. A. Palamarchuk, "Effect of die radii on material waste during equal channel angular extrusion," *Materials and Manufacturing Processes*, vol. 28, no. 8, pp. 910–915, 2013.

[11] A. V. Perig, I. G. Zhbankov, I. A. Matveyev, and V. A. Palamarchuk, "Shape effect of angular die external wall on strain unevenness during equal channel angular extrusion," *Materials and Manufacturing Processes*, vol. 28, no. 8, pp. 916–922, 2013.

[12] A. V. Perig and A. M. Laptev, "Study of ECAE mechanics by upper bound rigid block model with two degrees of freedom," *Journal of the Brazilian Society of Mechanical Sciences and Engineering*, vol. 36, no. 3, pp. 469–476, 2014.

[13] A. V. Perig and N. N. Golodenko, "CFD simulation of ecae through a multiple-angle die with a movable inlet wall," *Chemical Engineering Communications*, vol. 201, no. 9, pp. 1221–1239, 2014.

[14] A. V. Perig and N. N. Golodenko, "CFD 2D simulation of viscous flow during ECAE through a rectangular die with parallel slants," *International Journal of Advanced Manufacturing Technology*, vol. 74, no. 5–8, pp. 943–962, 2014.

[15] A. V. Perig, "2D upper bound analysis of ECAE through 2θ-dies for a range of channel angles," *Materials Research*, vol. 17, no. 5, pp. 1226–1237, 2014.

[16] A. V. Perig, A. F. Tarasov, I. G. Zhbankov, and S. N. Romanko, "Effect of 2θ-punch shape on material waste during ECAE through a 2θ-die," *Materials and Manufacturing Processes*, vol. 30, no. 2, pp. 222–231, 2015.

[17] A. V. Perig and N. N. Golodenko, "ECAP process improvement based on the design of rational inclined punch shapes for the acute-angled Segal 2θ-dies: CFD 2-D description of dead zone reduction," *Mechanical Sciences*, vol. 6, no. 1, pp. 41–49, 2015.

[18] A. Perig, "Two-parameter rigid block approach to upper bound analysis of equal channel angular extrusion through a segal 2θ-die," *Materials Research*, vol. 18, no. 3, pp. 628–638, 2015.

[19] A. V. Perig and N. N. Golodenko, "CFD 2D description of local flow of polymer workpiece through a modified U-shaped die during equal channel multiple angular extrusion," *Materials Research*, vol. 19, no. 3, pp. 602–610, 2016.

[20] A. V. Perig and N. N. Golodenko, "Effect of workpiece viscosity on strain unevenness during equal channel angular extrusion: CFD 2D solution of Navier–Stokes equations for the physical variables "flow velocities—punching pressure"," *Materials Research Express*, vol. 3, no. 11, Article ID 115301, 2016.

[21] J. Qiu, T. Murata, X. Wu, M. Kitagawa, and M. Kudo, "Plastic deformation mechanism of crystalline polymer materials in the equal channel angular extrusion process," *Journal of Materials Processing Technology*, vol. 212, no. 7, pp. 1528–1536, 2012.

[22] Y. R. Seo and J.-I. Weon, "Manipulation of nanofiller and polymer structures by using equal channel angular extrusion," *Journal of the Korean Physical Society*, vol. 63, no. 1, pp. 114–119, 2013.

[23] H.-J. Sue, H. Dilan, and C. K.-Y. Li, "Simple shear plastic deformation behavior of polycarbonate plate due to the equal channel angular extrusion process. I: finite element methods modeling," *Polymer Engineering and Science*, vol. 39, no. 12, pp. 2505–2515, 1999.

[24] J. I. Weon, T. S. Creasy, H.-J. Sue, and A. J. Hsieh, "Mechanical behavior of polymethylmethacrylate with molecules oriented via simple shear," *Polymer Engineering & Science*, vol. 45, no. 3, pp. 314–324, 2005.

[25] Y. Wu and I. Baker, "An experimental study of equal channel angular extrusion," *Scripta Materialia*, vol. 37, no. 4, pp. 437–442, 1997.

[26] Z.-Y. Xia, H.-J. Sue, and T. P. Rieker, "Morphological evolution of poly(ethylene terephthalate) during equal channel angular extrusion process," *Macromolecules*, vol. 33, no. 23, pp. 8746–8755, 2000.

[27] X. Zhang, D. Gao, X. Wu, and K. Xia, "Bulk plastic materials obtained from processing raw powders of renewable natural polymers via back pressure equal channel angular consolidation (BP-ECAC)," *European Polymer Journal*, vol. 44, no. 3, pp. 780–792, 2008.

[28] K. Chijiiwa, Y. Hatamura, and N. Hasegawa, "Characteristics of plasticine used in the simulation of slab in rolling and continuous casting," *Transactions of the Iron and Steel Institute of Japan*, vol. 21, no. 3, pp. 178–186, 1981.

[29] J. W. Goodwin and R. W. Hughes, *Rheology for Chemists: An Introduction*, Royal Society of Chemistry, Cambridge, UK, 2008.

[30] P. Oswald, *Rheophysics. The Deformation and Flow of Matter*, Cambridge University Press, New York, NY, USA, 2009.

[31] R. A. Pethrick, *Polymer Structure Characterization: From Nano to Macro Organization*, RSC, Cambridge, UK, 2007.

[32] M. Rubinstein and R. H. Colby, *Polymer Physics*, Oxford University Pres, New York, NY, USA, 2003.

[33] H. Sofuoglu and J. Rasty, "Flow behavior of Plasticine used in physical modeling of metal forming processes," *Tribology International*, vol. 33, no. 8, pp. 523–529, 2000.

[34] G. Strobl, *The Physics of Polymers. Concepts for Understanding Their Structures and Behavior*, Springer, Berlin, Germany, 2007.

[35] P. J. Roache, *Computational fluid dynamics*, Hermosa Publishers, Albuquerque, NM, USA, 1976.